Study of quasielastic scattering using charged-current ν_μ-iron interactions in the MINOS near detector

P. Adamson,[7] I. Anghel,[14,1] A. Aurisano,[6] G. Barr,[20] M. Bishai,[2] A. Blake,[4] G. J. Bock,[7] D. Bogert,[7] S. V. Cao,[28] C. M. Castromonte,[8] S. Childress,[7] J. A. B. Coelho,[29,5] L. Corwin,[13] D. Cronin-Hennessy,[17] J. K. de Jong,[20] A. V. Devan,[31] N. E. Devenish,[26] M. V. Diwan,[2] C. O. Escobar,[5] J. J. Evans,[16] E. Falk,[26] G. J. Feldman,[9] M. V. Frohne,[10] H. R. Gallagher,[29] R. A. Gomes,[8] M. C. Goodman,[1] P. Gouffon,[23] N. Graf,[12] R. Gran,[18] K. Grzelak,[30] A. Habig,[18] S. R. Hahn,[7] J. Hartnell,[26] R. Hatcher,[7] A. Holin,[15] J. Huang,[28] J. Hylen,[7] G. M. Irwin,[25] Z. Isvan,[2,21] C. James,[7] D. Jensen,[7] T. Kafka,[29] S. M. S. Kasahara,[17] G. Koizumi,[7] M. Kordosky,[31] A. Kreymer,[7] K. Lang,[28] J. Ling,[2] P. J. Litchfield,[17,22] P. Lucas,[7] W. A. Mann,[29] M. L. Marshak,[17] N. Mayer,[29,13] C. McGivern,[21] M. M. Medeiros,[8] R. Mehdiyev,[28] J. R. Meier,[17] M. D. Messier,[13] W. H. Miller,[17] S. R. Mishra,[24] S. Moed Sher,[7] C. D. Moore,[7] L. Mualem,[3] J. Musser,[13] D. Naples,[21] J. K. Nelson,[31] H. B. Newman,[3] R. J. Nichol,[15] J. A. Nowak,[17] J. O'Connor,[15] M. Orchanian,[3] R. B. Pahlka,[7] J. Paley,[1] R. B. Patterson,[3] G. Pawloski,[17,25] A. Perch,[15] M. Pfützner,[15] S. Phan-Budd,[1] R. K. Plunkett,[7] N. Poonthottathil,[7] X. Qiu,[25] A. Radovic,[31,15] B. Rebel,[7] C. Rosenfeld,[24] H. A. Rubin,[12] M. C. Sanchez,[14,1] J. Schneps,[29] A. Schreckenberger,[17] P. Schreiner,[1] R. Sharma,[7] A. Sousa,[6,9] N. Tagg,[19] R. L. Talaga,[1] J. Thomas,[15] M. A. Thomson,[4] X. Tian,[24] A. Timmons,[16] S. C. Tognini,[8] R. Toner,[9,4] D. Torretta,[7] J. Urheim,[13] P. Vahle,[31] B. Viren,[2] J. J. Walding,[31] A. Weber,[20,22] R. C. Webb,[27] C. White,[12] L. Whitehead,[11,2] L. H. Whitehead,[15] S. G. Wojcicki,[25] and R. Zwaska[7]

(MINOS Collaboration)

[1]*Argonne National Laboratory, Argonne, Illinois 60439, USA*
[2]*Brookhaven National Laboratory, Upton, New York 11973, USA*
[3]*Lauritsen Laboratory, California Institute of Technology, Pasadena, California 91125, USA*
[4]*Cavendish Laboratory, University of Cambridge, Madingley Road, Cambridge CB3 0HE, United Kingdom*
[5]*Universidade Estadual de Campinas, IFGW-UNICAMP, CP 6165, 13083-970 Campinas, São Paulo, Brazil*
[6]*Department of Physics, University of Cincinnati, Cincinnati, Ohio 45221, USA*
[7]*Fermi National Accelerator Laboratory, Batavia, Illinois 60510, USA*
[8]*Instituto de Física, Universidade Federal de Goiás, CP 131, 74001-970 Goiânia, Goiás, Brazil*
[9]*Department of Physics, Harvard University, Cambridge, Massachusetts 02138, USA*
[10]*Holy Cross College, Notre Dame, Indiana 46556, USA*
[11]*Department of Physics, University of Houston, Houston, Texas 77204, USA*
[12]*Department of Physics, Illinois Institute of Technology, Chicago, Illinois 60616, USA*
[13]*Indiana University, Bloomington, Indiana 47405, USA*
[14]*Department of Physics and Astronomy, Iowa State University, Ames, Iowa 50011, USA*
[15]*Department of Physics and Astronomy, University College London, Gower Street, London WC1E 6BT, United Kingdom*
[16]*School of Physics and Astronomy, University of Manchester, Oxford Road, Manchester M13 9PL, United Kingdom*
[17]*University of Minnesota, Minneapolis, Minnesota 55455, USA*
[18]*Department of Physics, University of Minnesota Duluth, Duluth, Minnesota 55812, USA*
[19]*Otterbein College, Westerville, Ohio 43081, USA*
[20]*Subdepartment of Particle Physics, University of Oxford, Oxford OX1 3RH, United Kingdom*
[21]*Department of Physics and Astronomy, University of Pittsburgh, Pittsburgh, Pennsylvania 15260, USA*
[22]*Rutherford Appleton Laboratory, Science and Technology Facilities Council, Didcot OX11 0QX, United Kingdom*
[23]*Instituto de Física, Universidade de São Paulo, CP 66318, 05315-970 São Paulo, São Paulo, Brazil*
[24]*Department of Physics and Astronomy, University of South Carolina, Columbia, South Carolina 29208, USA*
[25]*Department of Physics, Stanford University, Stanford, California 94305, USA*
[26]*Department of Physics and Astronomy, University of Sussex, Falmer, Brighton BN1 9QH, United Kingdom*
[27]*Physics Department, Texas A&M University, College Station, Texas 77843, USA*
[28]*Department of Physics, University of Texas at Austin, 1 University Station C1600, Austin, Texas 78712, USA*
[29]*Physics Department, Tufts University, Medford, Massachusetts 02155, USA*
[30]*Department of Physics, University of Warsaw, Hoża 69, PL-00-681 Warsaw, Poland*
[31]*Department of Physics, College of William & Mary, Williamsburg, Virginia 23187, USA*

(Received 30 October 2014; published 8 January 2015)

Kinematic distributions from an inclusive sample of 1.41×10^6 charged-current ν_μ interactions on iron, obtained using the MINOS near detector exposed to a wide-band beam with peak flux at 3 GeV, are compared to a conventional treatment of neutrino scattering within a Fermi gas nucleus. Results are used to guide the selection of a subsample enriched in quasielastic ν_μFe interactions, containing an estimated 123,000 quasielastic events of incident energies $1 < E_\nu < 8$ GeV, with $\langle E_\nu \rangle = 2.79$ GeV. Four additional subsamples representing topological and kinematic sideband regions to quasielastic scattering are also selected for the purpose of evaluating backgrounds. Comparisons using subsample distributions in four-momentum transfer Q^2 show the Monte Carlo model to be inadequate at low Q^2. Its shortcomings are remedied via inclusion of a Q^2-dependent suppression function for baryon resonance production, developed from the data. A chi-square fit of the resulting Monte Carlo simulation to the shape of the Q^2 distribution for the quasielastic-enriched sample is carried out with the axial-vector mass M_A of the dipole axial-vector form factor of the neutron as a free parameter. The effective M_A which best describes the data is $1.23^{+0.13}_{-0.09}(\text{fit})^{+0.12}_{-0.15}(\text{syst})$ GeV.

DOI: 10.1103/PhysRevD.91.012005 PACS numbers: 13.15.+g, 14.20.Dh, 25.30.Pt, 95.55.Vj

I. INTRODUCTION

Recent measurements of neutrino interactions in nuclei have challenged our understanding of how neutrino-nucleon scattering is modified when the target nucleons are entangled within a nuclear binding potential. Cross section discrepancies relative to ν_μN and $\bar{\nu}_\mu$N scattering on free nucleons are particularly apparent for charged current (CC) neutrino-nucleus interactions initiated by neutrinos in the energy range of E_ν from 0.5 to a few GeV [1–9]. Meanwhile, the accuracy of neutrino interaction models is becoming increasingly important to the analysis of neutrino flavor oscillation experiments, especially for CC interactions. The detector configurations deployed in neutrino oscillation experiments have given rise to new, high statistics neutrino scattering measurements on carbon and oxygen nuclei. The results to date have made it clear that models tuned primarily on light-liquid bubble-chamber data do not provide precise descriptions of neutrino-nucleus interactions [10,11].

The present work seeks to shed light on CC $\nu_\mu A$ scattering in the region $1 < E_\nu < 8$ GeV. For this purpose, an overview of inclusive CC scattering is established by comparing data of selected event samples to the predictions of a conventional Monte Carlo (MC) treatment wherein neutrinos interact with the nucleons of a relativistic Fermi gas. These samples are used to guide an analysis of charged-current quasielastic (CCQE) scattering,

$$\nu_\mu + \mathrm{n} \rightarrow \mu^- + \mathrm{p}, \tag{1}$$

the fundamental semileptonic interaction that features prominently in many neutrino oscillation measurements.

In contrast to nearly all previous works, the target neutrons of this study are bound within the large iron ($A \simeq 56$) nucleus [12]. The neutrino energy spectrum analyzed here overlaps and extends the E_ν region studied by K2K [1,2], MiniBooNE [3,5], SciBooNE [6], and T2K [7]. It extends to the beginning of the high energy region studied by NOMAD (with average E_{ν_μ} of 25.9 GeV) [4]; it coincides very nearly with the ν_μ spectrum investigated by MINERνA [9]. Thus, the observations pertaining to CCQE interactions in ν_μFe collisions reported here are complementary to information gleaned from CCQE scattering on $A \simeq 12$, 16 nuclei.

The neutrino interactions of this work were recorded in the MINOS near detector using an exposure to the NuMI neutrino beam at Fermilab operated in its low-energy configuration. Particular attention is devoted to event distributions in the (positive) square four-momentum transfer between the neutrino and the target nucleon, $Q^2 = -q^2 = -(k_\nu - k_\mu)^2 > 0$, where $k_\mu(k_\nu)$ is the four-momentum of the outgoing (incoming) lepton. High-statistics Q^2 distributions of selected CC samples are compared to the predictions of conventional neutrino scattering phenomenology as encoded into the MC event generator NEUGEN3 [13] used by the MINOS experiment. The neutrino interaction model of NEUGEN3 provides an overall characterization of neutrino CC interactions at incident energies of a few GeV. The analysis makes use of fits to the shapes of Q^2 distributions in the selected event samples. Information about the event rate is not used to constrain model parameters in order to avoid the sizable uncertainties associated with the absolute normalization of the neutrino flux.

The analysis uses a conventional neutrino-generator description of final-state initiation and evolution. In particular, CCQE signal events are taken to be quasielastic interactions on quasifree neutrons prior to final-state interactions. This simplified, somewhat naive formalism allows CCQE scattering in iron to be parametrized using the axial-vector mass, M_A, while avoiding the complexities inherently present in interactions on nuclei. The downside is that the M_A value determined from the data is an effective parameter only indirectly related to the axial-vector form factor of the neutron. However, since previous work in this field was based on similar formalism, the approach taken

here allows straightforward comparison of its determination for ν_μFe scattering to previous M_A results obtained with light target nuclei.

II. OUTLINE

The paper proceeds as follows: Sec. III summarizes the role of the axial-vector form factor and of the axial mass parameter, M_A, in quasielastic scattering, and summarizes the recent experimental determinations of an effective M_A for CCQE interactions in nuclear targets. Sections IV and V present the relevant aspects of the NuMI neutrino beam, of the MINOS near detector, and of the data exposure. The neutrino interaction model used by the reference MC is described in Sec. VI. The main interaction categories invoked by the model are quasielastic scattering, CC baryon resonance production for which production of $\Delta(1232)$ states is predominant, and CC deep-inelastic scattering including low-multiplicity pion production. Other relatively low-rate channels are also treated.

Upon isolation of a large CC inclusive data sample (1.41×10^6 events), the analysis commences with comparisons of kinematic distributions to MC predictions (Sec. VII). The MC categorizations serve to guide the extraction of four independent subsamples from the inclusive sample, whose events populate topological and kinematic sideband regions to CCQE scattering (Sec. VIII).

In subsamples containing abundant CC baryon resonance production, the MC predicts event rates which exceed the data rates for the region $0 < Q^2 < 0.5$ GeV^2. The data of the sideband samples are used to develop a Q^2-dependent suppression weight for baryon resonance production (Sec. VIII C). This weight is subsequently included as a refinement to the MC model, thus modifying the predicted amount of baryon-resonance background at low Q^2 in the CCQE enhanced sample. The latter sample, selected to be enriched in quasielastic events, is presented in Sec. IX.

The effective axial-vector mass is determined by fitting the shape of the Q^2 distribution of the CCQE enhanced sample. The data-fitting framework to do this is presented in Sec. X. Evaluation of the sources of systematic uncertainty for the M_A determination is presented in Sec. X C. Final results are given in Sec. XI and implications are discussed.

III. CC QUASIELASTIC SCATTERING

The CCQE differential cross section with respect to the squared four-momentum transfer between the leptonic and hadronic currents, Q^2, follows the general form

$$\frac{d\sigma}{dQ^2} = \frac{M_n^2 G_F^2 \cos^2(\theta_c)}{8\pi E_\nu^2} \times \left\{ A(Q^2) + B(Q^2)\frac{(s-u)}{M_n^2} + C(Q^2)\frac{(s-u)^2}{M_n^4} \right\}. \quad (2)$$

Here, $(s-u) = 4E_\nu M_n - Q^2 - m_\mu^2$, where M_n is the mass of the struck neutron and m_μ is the mass of the final-state muon. The functional forms $A(Q^2)$, $B(Q^2)$, and $C(Q^2)$ contain terms with various combinations of the nucleon vector form factors and the nucleon axial-vector form factor $F_A(Q^2)$; their explicit forms are given in Ref. [14]. [For antineutrino CCQE scattering, $M_n \to M_p$ and the sign of $B(Q^2)$ is reversed.] Additionally there are terms within $A(Q^2)$ and $B(Q^2)$ which contain the pseudoscalar form factor $F_P(Q^2)$. These however have a negligible effect in the present analysis and are ignored. According to conventional phenomenology the vector form factors satisfy the conserved vector current (CVC) hypothesis [15] and therefore are directly related to the Sachs electric and magnetic form factors [16]. The latter form factors have been well measured by electron scattering experiments. The coupling strength of the axial-vector form factor at zero four-momentum transfer, $F_A(Q^2 = 0)$, is well known from neutron β-decay experiments. Consequently a full description of the differential cross section for CCQE scattering hinges upon determination of the axial-vector form factor, $F_A(Q^2)$. The form factor's falloff with increasing Q^2 is conventionally parametrized using the empirical dipole form

$$F_A(Q^2) = F_A(0)/(1 + Q^2/M_A^2)^2. \quad (3)$$

Thus the axial-vector form factor can be described with just one parameter, the axial-vector mass, M_A. The magnitude of M_A determines the shape of the Q^2 momentum transfer spectrum and sets the scale for the absolute CCQE cross section $\sigma(E_\nu)$ (hence the total CCQE rate in an experiment) as well.

The value of M_A can be extracted by measuring the Q^2 distribution for CCQE scattering events. One decade ago, the world-average value for M_A was (1.026 ± 0.021) GeV [17]; this value was dominated by measurements obtained using large-volume bubble chambers filled with liquid deuterium such as those operated at the Argonne [18] and Brookhaven [19] National Laboratories. More recent experiments use parametrizations of vector form factor measurements obtained by electron scattering experiments, a refinement that shifts M_A to the lower value of 0.99 GeV [20].

In recent times, high-statistics experiments using tracking spectrometers have studied the CCQE interaction using nuclear targets. The K2K experiment reported an M_A value of (1.20 ± 0.12) GeV using oxygen as the target nuclei [1] and the MiniBooNE experiment measured (1.35 ± 0.17) GeV using carbon as the target medium [5]. On the other hand the NOMAD experiment, working in a distinctly higher E_ν range, obtained $M_A = (1.05 \pm 0.06)$ GeV, a value consistent with the bubble chamber results [4]. A widely held viewpoint is that the apparent spread in M_A values is driven by nuclear medium alterations of the CCQE free-nucleon cross section [10,21].

The MINERνA experiment has reported flux-averaged $d\sigma/dQ^2$ distributions for both neutrino and antineutrino quasielastic scattering on carbon [8,9]. The distributions span the energy range $1.5 < E_\nu < 10$ GeV and thereby bridge the ranges examined by other recent experiments. Satisfactory fits are obtained for both data sets using a relativistic Fermi gas (RFG) nuclear model with $M_A = 0.99$ GeV. However, augmentation of the RFG model with the transverse enhancement model (TEM) [22] improves the description. The TEM involves a distortion to the magnetic form factors for bound nucleons, a phenomenological result extracted from electron-carbon scattering data and applied directly to the same magnetic form factor in the neutrino case.

There are other phenomenological models which deduce the effects of the nuclear medium on CCQE scattering based on knowledge of electron-nucleus scattering. These models build upon RFG and include the final-state suppression resulting from Pauli exclusion of the reaction proton from occupied levels of the target nucleus. The effect of Pauli blocking on CCQE is significant; in a large nucleus such as iron the suppression extends from 0.0 to $\sim$0.3 GeV^2 in Q^2.

Current models include contributions due to multinucleon effects such as nucleon-nucleon correlations and two-particle two-hole (2p2h) processes [23–30]. These additional processes can initiate scattering events which, in many experiments, would appear to be CCQE-like and would distort the CCQE cross section. In one approach, the differential and total cross sections for CCQE are calculated as the squared sum of all microscopic interaction amplitudes devoid of pion emission, including reaction (1) [24,30,31]. Another approach is to use scaling arguments to estimate component contributions in electron scattering data and then to apply them to neutrino processes [27,28]. Among recent works, Ref. [30] obtains a description of MINERνA data comparable to the models presented with those measurements, while also describing the MiniBooNE measurement [29].

In a recent measurement reported by MINERνA, a conventional Fermi gas treatment of nuclei is found to give a poor description of the evolution of event rates with target A (from C to Fe to Pb), for CC scattering samples having sizable quasielastic contributions [32]. This observation suggests that nuclear medium effects may become more pronounced in neutrino CCQE scattering when relatively large nuclei are used. Given that most of the phenomenological approaches described above are applicable to larger nuclei, new measurements of CCQE scattering from a large-A nucleus such as iron are of keen interest.

IV. NuMI NEUTRINO BEAM

The neutrino beam used in this measurement is produced by the NuMI facility at Fermilab [33]. Protons with energy of 120 GeV are extracted from the main injector accelerator in an 8 μs spill every 2.2 s and directed onto a graphite target of length corresponding to 2.0 proton interaction lengths. The downstream end of the target was inserted 25 cm into the neck of the first (most upstream) of two focusing horns consisting of pulsed air-core toroidal magnets operated with a peak current of 185 kA. Positively charged pions and kaons produced in the target are focused towards the beam axis by the magnetic horns, and are directed into a 675 m long evacuated decay pipe. The neutrinos are produced by the subsequent decays of the mesons, as well as by decays of some of the daughter muons. The decay region is terminated by a hadron absorber. Residual muons are ranged out in the 240 m of rock between the absorber and the near detector. The near detector is located 1.04 km downstream from the target in a cavern 100 m underground.

To predict the neutrino flux and consequent event rate spectrum, the simulation package FLUKA05 [34] is used to calculate the production of secondary hadrons created by the collision of primary protons with the graphite target. The transport of these hadrons and of their decay products (primarily neutrinos, muons, pions, and kaons) along the NuMI beamline is then calculated using GEANT3 [35]. Interactions of the neutrinos striking the near detector are simulated using the NEUGEN3 neutrino event generator.

Refinements to the *ab initio* simulation of the beam flux at the detector are subsequently made using a fitting procedure in which the energy spectra of CC interactions observed in the detector are compared to predictions of the MC beam simulation. For this purpose, runs of short duration were taken in which the primary target was situated at positions displaced longitudinally from the nominal; the horn currents were also varied. With each distinct configuration of target location and horn currents, data are obtained for which the transverse and longitudinal momentum spectra of the hadrons focused by the horns are modified. Consequently the energy spectra for neutrino CC interactions at the detector are different for each run. This enables the simulated descriptions of transverse and longitudinal momentum distributions of produced π and K mesons to be adjusted so as to obtain the best agreement with the neutrino event rate spectrum of each run [36]. Hereafter, the MC calculation with the modifications described above is referred to as the *flux-tuned MC*.

An independent estimation of the neutrino flux for $E_\nu > 3.0$ GeV was carried out using a CC subsample characterized by low hadronic energy, to determine the flux shape [37]. The flux obtained is consistent throughout its E_ν range with the flux tune used by the present work.

The neutrino CC event energy spectrum for the entire data exposure, calculated using the flux-tuning procedure described above, is displayed in Fig. 1. Also shown is the small contribution (dashed line) arising from antineutrinos in the beam. For CC events in the near detector, the relative

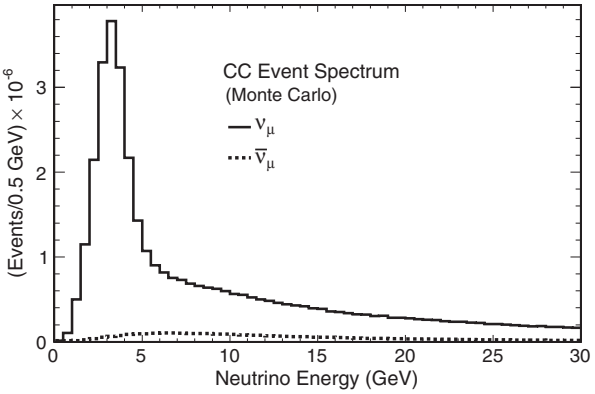

FIG. 1. Event rate spectra calculated for ν_μ (solid line) and $\bar{\nu}_\mu$ (dashed line) CC interactions in the near detector. The quasielastic events and other low multiplicity CC interactions selected by this analysis arise predominantly from the E_ν region of 1.5 to 6.0 GeV.

rates among neutrino flavors are estimated to be 91.7% ν_μ, 7.0% $\bar{\nu}_\mu$, and 1.3% $\nu_e + \bar{\nu}_e$.

V. DETECTOR AND DATA EXPOSURE

A. MINOS near detector

The near detector is a coarse-grained, magnetized tracking calorimeter composed of planes of iron and plastic scintillator [37,38]. The bulk of its 980 metric ton total mass resides in 282 vertically mounted steel plates. The upstream portion consisting of 120 planes comprises the detector's calorimeter section, while the remaining 162 planes deployed downstream serve as the detector's muon spectrometer. Each steel plate is 2.54 cm thick and corresponds to 0.15 nuclear absorption lengths and 1.4 radiation lengths. The scintillator planes are made of strips, 1 cm thick and 4.1 cm wide (1.1 Molière radii), oriented at ±45° with respect to the vertical and alternating ±90° in successive planes. The strips are read out with wavelength shifting fibers connected to multianode photomultiplier tubes (PMTs). The 120 planes of the calorimeter span a distance of 7.2 m along the beam direction, and the 162 planes of the spectrometer extend the tracking volume by an additional 9.7 m. (The pitch of the detector is 5.97 cm; it encompasses steel, scintillator module, and air gap.) In the muon spectrometer section, every fifth plane is instrumented with the scintillator but the intervening planes are bare steel with air gaps.

The steel planes are magnetized with a toroidal field of average strength 1.3 T, arranged to focus negative muons. The magnetic field enables the charges of final-state muons to be identified and provides a measurement of their momenta based upon track curvature. For muons that stop within the detector, the stopping distance provides an alternate, more accurate measure of the track momentum at the interaction vertex. In this work, events with exiting muons are included in the kinematic sideband samples; however muons of candidate quasielastic events are required to be negatively charged stopping tracks.

In the calorimeter section, every fifth plane is instrumented with a scintillator layer, while each of the four intervening planes has partial scintillator coverage over the area transverse to the beam. This is because, as shown in Fig. 2, the neutrino beam is centered between the axial hole that carries the magnet coil and the left side of the planes, and so the scintillator only needs to cover this area [38].

The relative locations of the event vertex fiducial region, the neutrino beam spot, the steel planes with the two types of scintillator coverage, and the magnet coil hole along the axis of the steel stack are shown in Fig. 2.

The neutrino interactions accepted for analysis occur in the forward part of the calorimeter section, in a fiducial volume defined as between 1 to 5 meters from the upstream end of the detector and within a 1 meter radius about the beam axis. The calorimeter section records the energy deposited by neutrino-induced hadronic showers. For the sub-GeV hadronic showers of interest to this analysis, the resolution for calorimetric measurement of hadronic shower energy is approximately 80% [38,39]. The downstream spectrometer section provides the curvature and range information required for reconstructing the momenta of muons from CC interactions in the calorimeter. For a 3.0 GeV muon, the energy resolution is 4.6% for measurement by range. Measurement by curvature has poorer resolution (11%) and is not used for the muon track reconstruction of candidate quasielastic events.

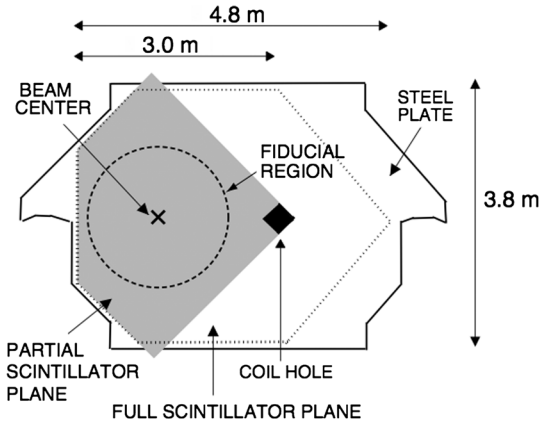

FIG. 2. Upstream transverse-face view of the MINOS near detector. The neutrino beam is centered between the axial-magnet coil hole and the left side of the stack of steel planes. The vertex fiducial volume is coaxial with the beam spot and begins at a longitudinal depth of 1.0 m within the calorimeter section. Every fifth steel plane is instrumented with a full scintillator plane (denoted by the dotted hexagonal border) while each of the four intervening planes has scintillator coverage as shown by the shaded region. The muon spectrometer section lies immediately downstream.

With measurement of track momentum from range, uncertainties arise from the detector mass, from approximations to the detector geometry used by the reconstruction software, and from the model of energy loss. These effects combine to give a 2% systematic error for range-based momentum.

B. Exposure, signal readout, calorimetric response

The data of this analysis are from an exposure totaling 1.26×10^{20} POT, taken in the first year of NuMI operation during 2005–2006. The average proton intensity was 2.2×10^{13} POT per accelerator spill of 8 μs duration. At this intensity, an average of eight neutrino interactions occur in the calorimeter region during each spill. For near detector ν_μ CC samples at this exposure the systematic errors of the measurement dominate the statistical errors (see Sec. X C).

To distinguish individual neutrino events in the detector from one another, both timing and spatial information are used. The readout electronics operate with essentially zero dead time. The PMT signals are continuously digitized throughout the spill in contiguous 18.8 ns intervals corresponding to the 53 MHz RF of the main injector.

Details concerning the calibrations required to convert raw PMT signals into deposited energy are given in Ref. [40]. The detector response to charged-particle traversal was measured by MINOS using a scaled-down 12 ton calorimeter having the same composition and granularity as the MINOS detectors. This replicate detector was exposed to beams of protons, pions, muons, and electrons in the momentum range 0.2 to 10 GeV, in a dedicated experiment at the CERN-PS [41].

VI. REFERENCE MONTE CARLO

The MINOS neutrino event generator NEUGEN3 provides descriptions of all the neutrino scattering processes that contribute to the event rate in the E_ν regime of this study. These include quasielastic scattering, baryon resonance production, low-multiplicity pion production, deeply inelastic scattering (DIS), and coherent pion production. The NEUGEN3 models for these processes are nearly identical to those of the GENIE (version 2.6.0) neutrino event generator [42]. Similar cross section categorizations are employed by other neutrino event generators currently in use such as NUANCE [43], NEUT [44], and NuWro [45].

For quasielastic scattering, NEUGEN3 uses the BBBA05 parametrization [46] of the nucleon vector form factors and the empirical dipole form for the axial-vector form factor computed with $F_A(0) = -1.267$ and with a nominal value for M_A of 0.99 GeV. A relativistic Fermi gas model of the nucleus includes the effects of Fermi motion and Pauli blocking. The RFG model is augmented with inclusion of a high-momentum tail to the distribution of nucleon momentum as proposed by Bodek and Ritchie [47]. This phenomenological augmentation allows a small number of MC events to exhibit kinematics which would not normally ensue with a RFG model; the occurrence of such events is predicted by spectral function models [48]. In the generation of νFe interactions by NEUGEN3, Pauli blocking is implemented as a rejection imposed upon generated quasielastic and elastic interactions whose recoil protons (or neutrons) are below 251 MeV/c (below 263 MeV/c). For generated events that survive the Pauli blocking step, the final-state hadrons are then propagated through the nuclear medium and probabilities are assigned to the possible rescatterings according to an intranuclear cascade algorithm INTRANUKE [49]. Via this particle cascade model, the detailed effects of pion and nucleon rescattering processes such as elastic and inelastic scattering, absorption, and charge exchange scattering are accounted for in simulations carried out by the reference MC.

In generation of neutrino-induced baryon resonance production decaying into the two-body final states (lepton + Δ/N^*), NEUGEN3 uses the phenomenological treatment of Rein and Sehgal [50]. This formalism takes into account the production of 18 different baryonic states in exclusive-channel reactions; the largest cross sections are those involving the charge states of the $\Delta(1232)$ resonance. For the $\Delta(1232)$ and for other baryon resonances as well, the axial-vector form factor is taken to be the empirical dipole form but with a mass value of $M_A^{\mathrm{RES}} = 1.12$ GeV [51]. For the present analysis (as with other MINOS studies), the NEUGEN3 generator does not impose Pauli blocking upon baryon resonance production. In the decay of the various resonance states, the emission of the daughter particles is assumed to proceed isotropically in the rest frame of the parent particle.

For its description of deep-inelastic scattering, NEUGEN3 uses the formalism of Bodek and Yang [52], including the extension of the formalism that improves the modeling of the transition region from resonance to DIS interactions [53]. A survey of neutrino interaction data from previous experiments was used to determine the appropriate hadronic mass spectrum (W spectrum) to use with events in this transition region. For events having hadronic mass between $1.7 < W < 2.0$ GeV, a good match to data distributions for $d\sigma/dW$ is achieved by implementing a linear evolution from the Rein-Sehgal exclusive channel treatment to the Bodek-Yang DIS model. For the production of multiparticle hadronic systems as occurs with DIS events, two different approaches are employed. For production of relatively low hadronic masses, final-state particle multiplicities are simulated according to a modified form of KNO scaling [54]. For higher invariant masses, e.g. $W > 2.3$ GeV, the KNO hadronic shower model is evolved into a PYTHIA/JETSET description [55].

The production of single pions via CC coherent scattering on iron is a background for the present study, for events in which the final-state pion goes undetected. NEUGEN3

simulates this process using an implementation of the PCAC-motivated coherent scattering model of Rein and Sehgal [56]. The cross section for this process is known to be small, and in fact its contribution as a background into the lowest Q^2 bins for selected CCQE events is estimated by NEUGEN3 to be 1%. The systematic error arising from the particular coherent scattering implementation is negligible compared to other errors in this analysis.

The reference MC uses a materials assay of the MINOS near detector to determine its nuclear composition. According to the MC, approximately 5% of the neutrino interactions recorded in the detector occur not on iron, but on the plastic scintillator and its aluminum skin. This 5% contribution to the event rate is included in the MC simulations with appropriate modifications made to the nuclear Fermi gas model for the carbon, hydrogen, and aluminum nuclei, and to the treatment of intranuclear rescattering in these lighter, smaller nuclei.

VII. CC ν_μ INCLUSIVE EVENT SAMPLE

A. Selection of the sample

The foundational sample for the analysis is an inclusive sample of ν_μ CC events selected from the data; the same selections are applied to a realistic Monte Carlo simulation of the experiment. The selection criteria used are mostly those used previously for the MINOS measurement of ν_μ disappearance oscillations and are described in detail in [57,58]. In brief, the presence or absence of a muon track in each event is ascertained using a multivariate likelihood discriminant. The discriminant assigns a probability for the muon hypothesis based upon four measured variables, namely the average pulse height per plane along the track, the transverse energy deposition along the track, the fluctuation of the energy deposits strip by strip along the track, and the length of the track. A track is required to traverse six or more scintillator planes, giving a muon energy threshold of 300 MeV. The sample includes events with exiting as well as stopping muon tracks.

To the above selections, the analysis adds additional data quality requirements: (i) A timing isolation cut is imposed; events in the calorimeter section that are concurrent within 70 ns with another event are excluded. This criterion eliminates instances of event pileup which occasionally lead to erroneous reconstructions. (ii) Events for which the muon track either ends on the far side of the axial hole which carries the energizing coil (transverse locations to the right of the coil hole in Fig. 2) or else stops within 45 cm of its center, are rejected.

The efficiency with which CC events are selected is found to be 87% in the MC simulation. The detection efficiency remains nearly constant with increasing muon angle with respect to the beam up to 35° and falls off rapidly at larger angles. The events retained include 92% of genuine CCQE events and 85% of two-body CC final states $\mu^- + \Delta/\mathrm{N}^*$.

B. Kinematic variables; muon angular resolution

The recoiling hadronic systems of CC events often give rise to scintillator "hits" that are clearly associated with the events but are not ionizations due to the muon tracks. The total summed pulse height from the hadronic shower hits in an event is used to estimate the system energy, hereafter designated as E_{had}.

Prerequisites for this estimation are parametrizations of the detector response to energies of single hadrons and photons. Such parametrizations have been developed by MINOS; they are based on simulations that have been cross-checked against calibration data obtained from test beam exposures of a replicate detector to protons, pions, and electrons [38]. The mapping of pulse height to E_{had} is completed using modeling of hadronic showers. The detector-response parametrizations are used in conjunction with estimations of the particle content of CC-induced hadronic systems, e.g. the particle types, multiplicities, and energies. For CC events having $200 < E_{\mathrm{had}} < 250$ MeV, a region of particular interest to the analysis, the mean multiplicities per event (according to the reference MC) are 1.9 protons, 1.3 neutrons, 0.4 $\pi^{\pm}$, and 0.1 π^0 mesons.

For simulated CCQE events in this E_{had} range, the mean of reconstructed E_{had} values falls within 6% of the mean for MC true values.

The distribution of reconstructed energies of the final-state hadronic systems, E_{had}, in events of the CC inclusive sample is shown in Fig. 3. The data events (solid circles) are displayed together with the predictions from the

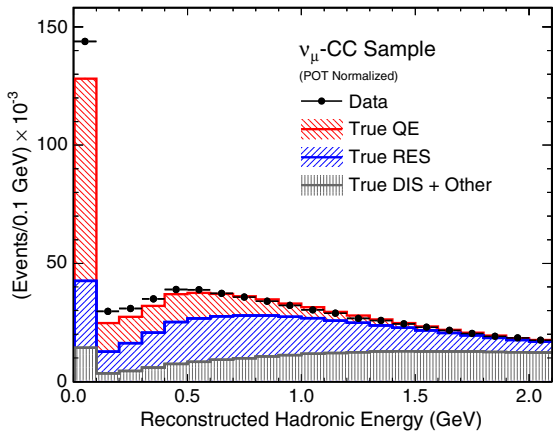

FIG. 3 (color online). Distribution of final-state hadronic energy, E_{had}, recoiling from the muon track in events of the inclusive CC samples of data (solid circles) and the flux-tuned MC (histograms). Subsamples of CCQE and CC baryon resonance channels as estimated by the MC are shown by the two elevated, hatched histograms (distributions are stacked). The remaining subsample (lowest, shaded) arises from CC nonresonant pion production and low-multiplicity DIS reactions.

flux-tuned MC for the same total exposure. For $E_{\rm had}$ bins above 500 MeV, the MC prediction agrees with the hadronic energy distribution. For the lower energy bins however, where CCQE is the dominant interaction, there is a relative excess of data; the MC underestimates the data rate by ∼11%.

The extent to which the reference MC simulation describes the CC inclusive sample is of general interest. Additional comparisons are afforded by the following kinematic estimators:

$$E_\nu^{(\rm est)} = E_\mu + E_{\rm had}, \tag{4}$$

and

$$Q^2 = 2E_\nu^{(\rm est)}(E_\mu - p_\mu \cos\theta_\mu) - m_\mu^2. \tag{5}$$

From Eq. (5) it can be seen that reconstruction of the muon angle, θ_μ, is important for the calculation of Q^2. In MINOS, the resolution, $\sigma(\theta_\mu)$, ranges between 16 mrad and 52 mrad for muons of the highest momenta (long tracks) and lowest momenta (short tracks), respectively. The angular resolution in the MC was compared to the data using two different methods. In one method the reconstructed angles of upstream vs downstream segments were compared at track midpoints, separately for muons from the data and the MC. In the other method, angles of track segments reconstructed in the near detector were compared with the reconstructed angle of the same tracks as they exit the upstream MINERνA detector [59]. Both methods showed the data to have better muon angular resolutions than were represented in the MC. The discrepancy was largest for short tracks ($p_\mu < 2$ GeV/c, $\bar{\sigma} = 52$ mrad), with reduction (in quadrature) of ∼14 mrad of smearing from the MC being required to match the data. However it diminished steadily with increasing track length, becoming indiscernible for tracks longer than 130 sampling planes ($p_\mu > 5$ GeV/c). This effect was shown to be unrelated to uncertainties with detector alignment; rather, it is attributed to cumulative errors in the MC model of detector response.

The MC-vs-data angular resolution discrepancy gives rise to a mild flattening of MC Q^2 distributions whose form is determined as follows: A randomized smearing of reconstructed angles is applied to muon tracks of data to obtain a sample having the resolution of the MC. The ratio of original to smeared data is constructed in bins of Q^2; the ratio exhibits a regular dependence which is well described using a polynomial function. The MC (bin by bin in Q^2) is then divided by values of the ratio function to obtain a MC distribution that would ensue if its resolution was identical to that of the data. Thus the ratio function serves as a correction weight which, hereafter, is applied to individual MC events according to their Q^2 values [60].

Ratio functions are determined separately for the CC inclusive sample, for the sideband subsamples, and for the CCQE enhanced sample; however there are only small differences among these functions. For all samples, the correction to the MC Q^2 distribution amounts to 3% as Q^2 approaches 0.0 and $< 2\%$ for all higher values. The uncertainties in MC-vs-data resolution differences per bin of track length imply a range of variation allowed to the correction weight. The one-sigma error band calculated for the weight is used to assign a systematic error to this correction.

The resolution in Q^2 [or $Q^2_{\rm QE}$ of Eq. (8)] is as follows: For $Q^2(Q^2_{\rm QE})$ below 0.05 GeV^2, the resolution is 0.03(0.02) GeV^2. At larger Q^2 $(Q^2_{\rm QE})$ the resolution increases to 0.08(0.07) GeV^2 at 0.25 GeV^2 and 0.13(0.11) GeV^2 at 0.45 GeV^2. For $Q^2 > 0.5$ GeV^2, the fractional resolution, $(Q^2_{\rm reco} - Q^2_{\rm true})/Q^2_{\rm true}$, is constant at 28% (25%) of Q^2 $(Q^2_{\rm QE})$ [61].

C. Kinematic distributions: Data vs the MC

Figure 4 compares the CC inclusive data to the MC prediction for event distributions in reconstructed E_ν and Q^2 (upper, lower plots respectively). The flux-tuned MC prediction is normalized using the total protons on target for the data exposure (POT normalization). The relative contributions from quasielastic scattering and from the two other dominant interaction categories are shown by the component (hatched) histograms. The MC (histogram upper boundary) is seen to provide first-order characterizations of the data distributions (solid circles).

A modest but useful degree of separation among the quasielastic, baryon resonance, and deep-inelastic scattering categories is provided by the final-state hadronic mass, W, reconstructed event by event in this analysis using the relation

$$W^2 = M_n^2 + (2M_n E_{\rm had}) - Q^2. \tag{6}$$

Figure 5 shows the distribution of hadronic system invariant mass for the CC inclusive sample. MC predictions for the three major interaction categories are shown as stacked histograms; the predicted event rates are normalized to the data exposure. The fractional resolution is linearly proportional to W through the region 0.6 to 2.0 GeV, improving gradually with increasing W from 32% to 20%. Clearly discernible is the quasielastic peak at W values near the nucleon mass. The peak is comprised of low-Q^2 events with $E_{\rm had}$ approaching zero; event reconstruction smearing extends the data and MC distributions to values below M_n.

The top plot in Fig. 4 shows the residual data-vs-MC disagreement after the flux-tuning procedure. The flux tuning uses beam optics and hadron production parameters to obtain the apparent agreement with the total event rate at high energy (E_ν above 6.0 GeV). The lack of agreement around the spectral peak is not readily attributable to either the flux or cross section models, since the tuning

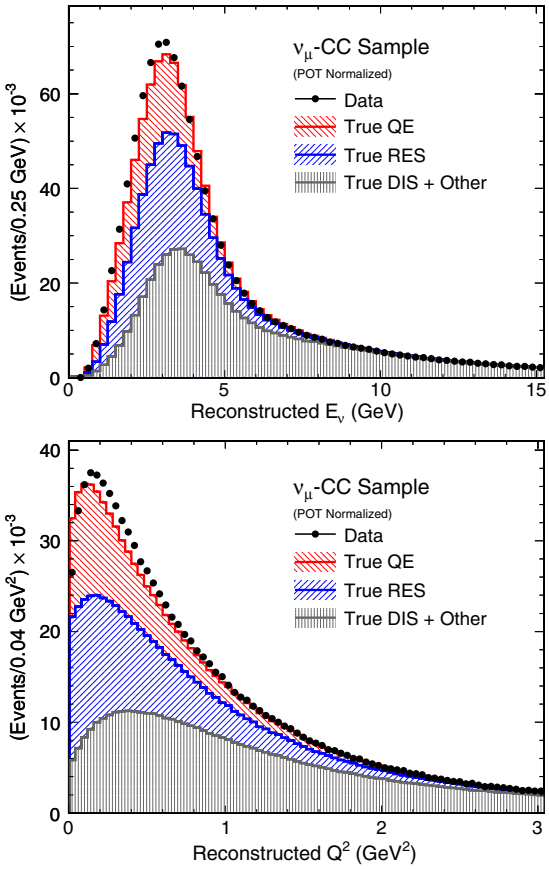

FIG. 4 (color online). Distributions of the CC inclusive sample in data (solid circles) and from the MC (histograms), for reconstructed neutrino energy (top) and for Q^2 (bottom). The component histograms (hatched, stacked) show MC predictions for contributions arising from quasielastic, baryon resonance production, and deep-inelastic scattering channels. The MC underestimates the rising edge of the neutrino energy distribution in data (top), and exhibits deviations from the shape of the data Q^2 distribution (bottom).

parameters will tend to compensate for shortcomings with either one. Note that CC DIS is the dominant process at high energy, and that data-vs-MC agreement correlates with the DIS event rate in all the distributions of Figs. 3, 4, and 5. On the other hand, the apparent data excess relative to the MC around the spectral peak, where CCQE and baryon-resonance production account for a large fraction of the event rate, correlates with apparent excesses in related regions of the other figures.

Despite the flux-tuning procedure, the data in Fig. 4 (bottom) exhibit a sharper falloff as Q^2 approaches zero than is predicted by the MC. This latter feature cannot be explained by uncertainties in the neutrino flux, or by uncertainties in the energy dependence of exclusive-channel cross sections, $\sigma(E)_{\mathrm{QE,RES}}$. Rather, such an effect is more naturally related to nuclear medium effects and/or form factor behavior, which is the physics targeted by the present analysis.

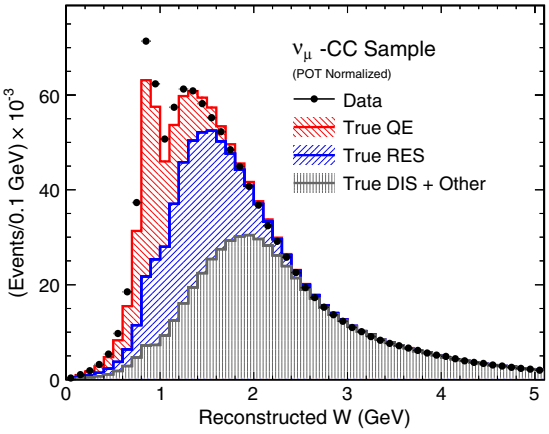

FIG. 5 (color online). Distribution of reconstructed hadronic mass W for events of the CC inclusive sample, compared to MC predictions for the main interaction categories (stacked histograms, normalized to the data exposure). The data exhibit an apparent excess relative to the MC in the region of the quasielastic peak; this feature is strongly correlated with the apparent data excess at $E_{\mathrm{had}} \simeq 0.0$ GeV seen in Fig. 3.

VIII. SELECTED CC SUBSAMPLES

The analysis seeks to isolate a subsample from the CC inclusive sample which is enriched in CCQE events. This subsample, referred to as the CCQE enhanced sample, serves as the CCQE signal sample for determination of the axial-vector mass and is presented in Sec. IX. Before obtaining the signal sample however, it is useful to elucidate the backgrounds that complicate the study of CCQE interactions. For these purposes, five mutually exclusive subsamples have been extracted from the CC inclusive sample. Four of these serve as kinematic sideband samples to CCQE, providing perspectives and constraints on background reaction categories, while the fifth subsample is the signal sample. An important development, described in Sec. VIII C, is the use of sideband samples enriched in CC baryon resonance production to develop a data-driven correction to the Q^2 distribution of that background reaction category.

A. Kinematic sideband samples

Nonquasielastic reactions capable of mimicking the CCQE topology in the MINOS detector consist of CC DIS events with low pion multiplicity and CC baryon resonance production events ($\mu^- + \Delta$ or N^* final states). The extent to which the NEUGEN3 neutrino generator accurately describes these background categories is investigated using four nonoverlapping subsamples from the CC inclusive event sample. Their extraction from the inclusive CC sample is based upon the hadronic mass W as follows:

(1) *High-Q^2 DIS sample*: Charged-current events of the deep-inelastic scattering regime are isolated by requiring $W > 2.0$ GeV. Events having $W > 2.0$ GeV

and $Q^2 > 1.0$ GeV^2 comprise the *high-Q^2 DIS sample*. According to the reference MC, this sample is completely dominated by true CC DIS events; however there is also a few percent contribution from CC baryon resonance production.

(2) *Low-Q^2 DIS sample*: Events having hadronic mass $W > 2.0$ GeV and $Q^2 < 1.0$ GeV^2 comprise the *low-Q^2 DIS sample*. According to the MC, this sample is also dominated by CC DIS events; however the fraction of CC baryon resonance production events is larger ($\sim$10%) than is the case for the high-Q^2 DIS sample.

(3) *RES-to-DIS transition sample*: Selection of events having hadronic invariant mass within the interval $1.3 < W < 2.0$ GeV isolates a baryon resonance-to-DIS transition sample, referred to hereafter as the *RES-to-DIS transition sample*.

(4) *QE-RES enriched and RES-enhanced samples*: Selection of CC events having $W < 1.3$ GeV yields a sample which is dominated by the quasielastic and baryon resonance production channels (hereafter, the *QE-RES enriched sample*). A cut on the energy of the hadronic shower recoiling from the muon, $E_{\rm had}$, is used to separate this sample into two subsamples, according to whether $E_{\rm had}$ falls above or below 250 MeV. The subsample for which $E_{\rm had}$ is greater than 250 MeV is referred to as the CC *RES-enhanced sample*. In the Q^2 region $0.0 < Q^2 < 0.5$ GeV^2, the reference MC predicts the latter sample to be dominated by baryon resonance production with the $\Delta(1232)^{++}$ being the most abundant baryon resonance state. This sample also contains a sizable CCQE component at moderate and high Q^2.

B. Sideband Q^2 distributions

1. Restriction to shape-only comparisons

The overall normalization of the absolute neutrino flux for this exposure is known to have an uncertainty of order 10%. This systematic is dominated by uncertainties in the modeling of hadron production from the graphite target [62,63]. Additionally there are uncertainties associated with the shape of the flux spectrum in regions most relevant to this analysis. To avoid these significant sources of error and their complicated systematics, the analysis forgoes inferences based upon differences in total event rate between data and the MC predictions. Rather, the approach taken is to restrict to shape-only comparisons, with emphasis placed upon the distributions of selected CC sideband and signal event samples in four-momentum transfer, Q^2. Consequently, in all subsequent figures showing MC comparisons to data, the MC prediction is shown scaled to the same number of events as in the data for the kinematic range displayed in each plot. The scaling of the MC in this way is denoted in all cases by the plot interior label "(Area Normalized)." For subsamples in which the CCQE component is sizable (the QE-RES enriched, RES-enhanced, and CCQE enhanced samples), the scale factors (MC/data) which map POT normalization into area normalization fall within the range 1.08 to 1.19.

2. Data vs MC

The combined Q^2 distribution of the two DIS samples is displayed in Fig. 6. The MC prediction is shown scaled to the same number of events as the data; the MC/data scale factor in this case is 0.98. This comparison checks the verity of the MC DIS model for CC interactions with $W > 2.0$ GeV, a region of hadronic mass lying well above the range $W < 1.3$ GeV from which CCQE candidate events are selected. For the high-Q^2 DIS sample, the MC is observed to match the data shape (and its absolute rate as well), for Q^2 from 2.0 to above 5.0 GeV^2 (beyond the range displayed in Fig. 6). Below 2.0 GeV^2 and throughout the region of the low-Q^2 DIS sample, the MC describes the general trend of the data (histogram vs solid circles); however there are discrepancies. These are indicative of shortcomings in the MC DIS model which may affect the small DIS component ($\sim$11%) estimated to reside in the selected signal sample. They comprise a source of systematic uncertainty whose presence is encompassed by error ranges allotted to parameters of the DIS model (Sec. X C 6).

The Q^2 distributions of data and MC for the RES-to-DIS transition sample are shown in Fig. 7, with the MC scaled to the total number of data events over the Q^2 range displayed. The transition sample is predicted by the MC to be

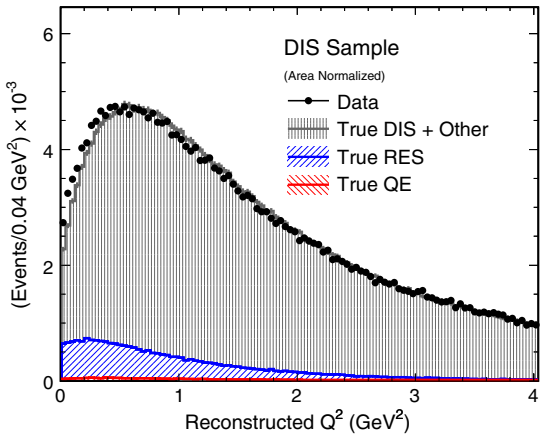

FIG. 6 (color online). Combined distribution of reconstructed Q^2 for events of the high-Q^2 DIS and low-Q^2 DIS samples (distributions above, below 1.0 GeV^2 respectively). The samples probe the MC model for DIS reactions of hadronic mass $W > 2.0$ GeV. The MC prediction (histograms, stacked) describes the general trend of the data (solid circles) but with discrepancies which reflect uncertainties in parameters of the DIS model.

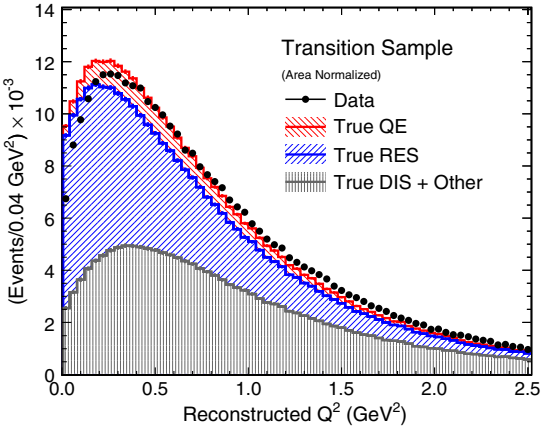

FIG. 7 (color online). Distribution of reconstructed Q^2 for events of the RES-to-DIS transition sample ($1.3 < W < 2.0$ GeV). The MC prediction (stacked histograms) is normalized to the number of data events. The MC spectrum lies above the data over the low-Q^2 region dominated by CC baryon resonance channels.

dominated by CC baryon resonance production throughout the low-Q^2 region from 0 to ~0.5 GeV^2. The MC exhibits an excess of event rate relative to the data throughout this low-Q^2 region.

Selection of CC events having $W < 1.3$ GeV yields the QE-RES enriched sample, from which the RES-enhanced sample is subsequently drawn. The Q^2 distributions for the parent QE-RES enriched sample and for the "daughter" RES-enhanced sample are shown in the upper and lower plots of Fig. 8, with the MC predictions (stacked histograms) scaled to the number of data events in each plot. From the component MC histograms it can be seen that the DIS contribution is now smaller than the contributions from CCQE events and from CC baryon resonance production. The RES-enhanced sample (lower plot) and the parent QE-RES enriched sample as well (upper plot) possess a dropoff in rate at very low Q^2 that is not reproduced by the MC.

C. Suppression of baryon resonances at low Q^2

The agreement of the MC with the Q^2 data distributions of the sideband samples, and of the signal-enhanced sample as well, is significantly improved by introduction of suppression of baryon resonance production at low Q^2. (The DIS scattering model is not affected.) A low-Q^2 suppression effect for CC two-body $\Delta(1232)$ production which extends beyond $Q^2 \sim 0.3$ GeV^2 has been invoked in analyses of the MiniBooNE data [5,64,65]. (See also Ref. [66]). The proposed effect resembles the low-Q^2 suppression exhibited by treatments that go beyond the Fermi gas model, such as the random phase approximation (RPA) [23,24,67,68], nuclear spectral functions [69], or the relativistic distorted-wave impulse approximation (RDWIA) as calculated for CCQE interactions [70]. Since the $\Delta(1232)$ and higher mass

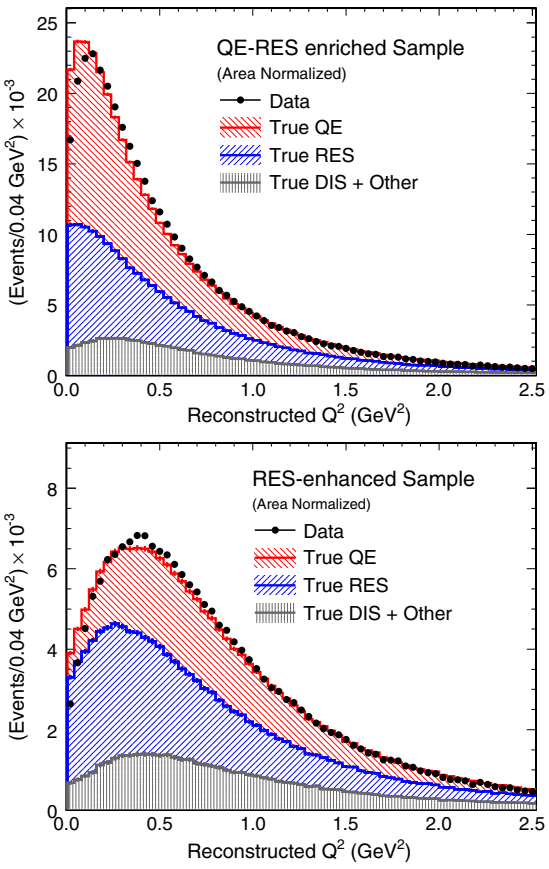

FIG. 8 (color online). Distributions of reconstructed Q^2 for the QE-RES enriched sample ($W < 1.3$ GeV) and for the RES-enhanced sample extracted from it by requiring $E_{\rm had} > 250$ MeV. MC predictions are normalized to data event rates; the stacked histograms show contributions by reaction category. The distribution shapes in data vs MC show differences, particularly at Q^2 near 0 GeV^2 where CC baryon resonance channels (middle hatched regions) dominate the event rate.

baryon resonance states are often too short-lived to escape the parent nucleus before decaying, Pauli blocking may account for part of this effect. As discussed below, the analysis finds that a suitable suppression factor is one that removes about 20% of two-body CC Δ/N^* production in the MC model. Of course the introduction of a suppression factor to be included in the MC model prediction has its own sources of uncertainty; these are accounted for in the error treatment of this analysis.

The RES-enhanced and RES-to-DIS transition samples were fitted together over the range $0 \le Q^2 < 0.6$ GeV^2 using a resonance suppression described as a function of true Q^2. The motivation is that, within this Q^2 range, baryon resonance production is the dominant reaction category in each sample. As described below, a similar functional shape is found to describe the suppression at low Q^2 in both samples.

The fitting to the two sideband samples was carried out as a multistep process. At the outset a candidate shape for

weighting to be applied in bins of true Q^2 was specified. The predicted contribution to each bin was then adjusted, one bin at a time, to a value that reduced the residuals over the two reconstructed samples after the samples were area-normalized. This yielded a suppression shape that better described the data. The next step was to fit an overall strength parameter in conjunction with the refined shape. The procedure for the two previous steps was then iterated and the change to the suppression parametrization was found to be negligible.

A systematic error band was constructed by evaluating the effects of error sources expected to be significant for the M_A^{QE} measurement. For Q^2 values below 0.3 GeV^2 the shape of the error band reflects uncertainties arising from the muon and hadron energy scales and from the intranuclear rescattering model, which affect event selection and Q^2 reconstruction. Also included is an allowance for sensitivity to higher-than-nominal M_A^{QE} values of the magnitude determined in this work. This sensitivity enters the construction of the suppression weight through the presence of CCQE background events in the sideband samples. At higher Q^2 the error band reflects uncertainty in the effective turnoff point for the suppression [71].

The suppression function with its error band is shown in Fig. 9. The function is applied to true baryon resonance events generated by the MC that enter the background estimate for the M_A^{QE} measurement. [For $0.0 < Q^2 < 0.7$ GeV^2, the central curve of Fig. 9 is replicated by the phenomenological form: $f(Q^2) = A \times [1 + \exp\{1 - \sqrt{Q^2}/Q_0\}]^{-1}$, with $A = 1.010$ and $Q_0 = 0.156$ GeV.] This data-driven suppression function remedies the discrepancy in the very low-Q^2 spectra of both the RES-enhanced and the RES-to-DIS transition sideband samples, two completely independent samples which contain very different admixtures of background processes.

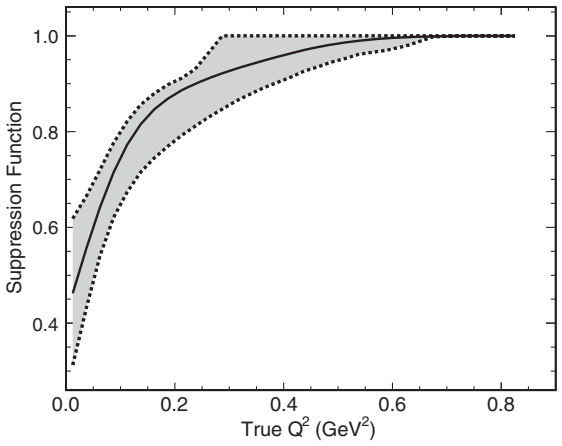

FIG. 9. The Q^2-dependent weight function which, when applied to the MC model of baryon resonance production, brings the MINOS MC predictions into agreement with data for sideband samples dominated by Δ/N^* production. The shape and strength of the suppression are sensitive to systematic uncertainties as indicated by the error band.

IX. CCQE ENHANCED SAMPLE

A. Event selection; CCQE kinematics

The final subsample to be drawn from the CC inclusive sample, one which has no overlap with the sideband samples, is the CCQE enhanced sample. Such a sample, enriched in signal events, is isolated by exploiting the tendency of CCQE interactions to deposit relatively small amounts of hadronic energy in the MINOS detector as illustrated by Fig. 3. The topology targeted is a single muon track, either with no additional energy deposition in the event or else with an accompanying hadronic system having E_{had} less than a few hundred MeV. Three criteria are used to select the candidate signal events of the CCQE enhanced sample:

(1) A selected event contains a single muon track (in accord with the criteria of Sec. VII A).
(2) The single reconstructed track is required to stop in the detector and not on the far side of the magnetic coil. The muon end point in alternate view planes must be separated by ≤ 5 planes (15 planes) for the calorimeter (spectrometer). At the far end of the spectrometer, the end point must be contained by at least two tracking planes.
(3) The reconstructed final-state hadronic system is required to have energy, E_{had}, less than a designated threshold value. As indicated by the distributions in Fig. 3, the threshold values of interest lie in the range $0 < E_{\mathrm{had}} < 500$ MeV. Based upon considerations of CCQE sample purity and the efficiency for retaining signal events, the selection threshold requirement for E_{had} is set to $E_{\mathrm{had}} < 225$ MeV.

The second criterion is motivated by the fact that in the MINOS near detector, determination of muon momentum by range yields a more accurate and higher resolution measurement than does measurement based upon track curvature. The second and third criteria constrain the kinematic distributions of the selected CCQE sample. The requirement that final-state muons stop in the detector effectively limits the sample to events with $E_\nu < 8$ GeV; the E_{had} restriction improves the sample purity but also removes genuine quasielastic events with large Q^2.

Reconstruction of muon momentum with good angular and momentum resolution is important because analysis of the CCQE enhanced sample can utilize a reconstruction of Q^2 based upon the QE hypothesis and muon kinematics, rather than relying on hadronic calorimetry as is done for the CC inclusive and the kinematic sideband samples. The neutrino energy and Q^2 can be estimated event by event by using the reconstructed muon track, under the assumption that each event is in fact a CCQE scatter from a stationary bound neutron. The expressions for these quantities, designated as E_ν^{QE} and Q^2_{QE}, are

$$E_\nu^{\rm QE} \equiv \frac{(M_n - \epsilon_B)E_\mu + (2M_n\epsilon_B - \epsilon_B^2 - m_\mu^2)/2}{(M_n - \epsilon_B) - E_\mu + p_\mu \cos\theta_\mu}, \quad (7)$$

and

$$Q^2_{\rm QE} \equiv 2E_\nu^{\rm QE}(E_\mu - p_\mu \cos\theta_\mu) - m_\mu^2. \quad (8)$$

For the reconstructed neutrino energy, $E_\nu^{\rm QE}$, the parameter $\epsilon_B = +34$ MeV accounts for the nucleon binding energy, or the average nucleon removal energy, of the target neutron within the iron nucleus. As an estimator of Q^2, $Q^2_{\rm QE}$ of Eq. (8) is unbiased for genuine CCQE events, but is biased towards lower values for the baryon resonance background reactions.

B. Selection efficiency and sample purity

Figure 10 shows the efficiency (solid-line histogram) and sample purity (dotted-line histogram) for the selected CCQE enhanced sample as a function of reconstructed $Q^2_{\rm QE}$. The efficiency is highest at $Q^2_{\rm QE} \simeq 0.0$; the residual 16% of inefficiency at $Q^2_{\rm QE} \simeq 0.0$ arises primarily from the muon containment requirement. The gradual falloff of efficiency with increasing $Q^2_{\rm QE}$ is due to the restriction imposed on the energy $E_{\rm had}$ of the recoiling hadronic system. In recognition of efficiency reduction at high $Q^2_{\rm QE}$, the fitting of the CCQE enhanced sample for M_A is restricted to events having reconstructed $Q^2_{\rm QE}$ in the range $0.0 < Q^2_{\rm QE} < 1.2$ GeV^2. The purity of the CCQE selected subsample exceeds 50% for all reconstructed $Q^2_{\rm QE}$ values below 1.2 GeV^2.

Event statistics for the CCQE enhanced sample together with an estimate of its reaction composition are presented in Table I. The populations of component CC reaction categories according to the MC model are tabulated in the upper rows. The lower rows show the MC predictions for the data exposure together with the numbers of data events. Also shown in the rightmost column are corresponding breakouts by reaction type, rates and ratios for the sample restricted by a selection ($E_\nu < 6.0$ GeV) which removes the high-E_ν tail of events. The data-over-MC ratio (bottom row) for either the full or restricted signal sample shows the observed candidate event rate to exceed the MC prediction by 19%.

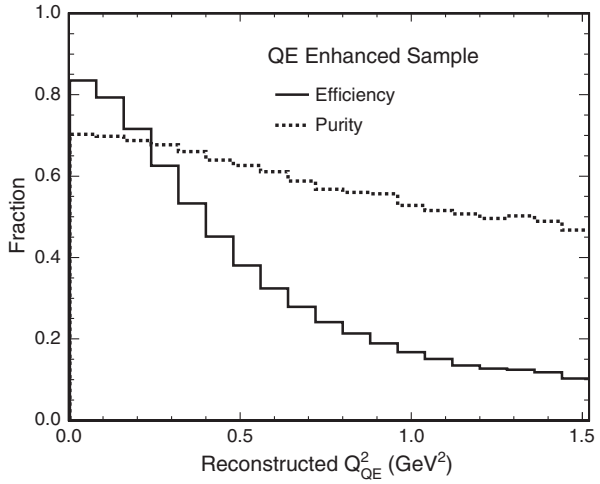

FIG. 10. The selection efficiency (solid-line histogram) and the purity (dotted-line histogram) for CCQE candidate events extracted from the CC inclusive sample, as a function of reconstructed Q^2. The falloff of efficiency with increasing $Q^2_{\rm QE}$ is a consequence of the restriction to low $E_{\rm had}$ events.

TABLE I. Event populations for the CCQE enhanced sample, in the MC model and in the data. Upper rows show the sample composition by reaction category as estimated by the MC model for the 1.26×10^{20} POT data exposure. Comparisons of the numbers of CCQE candidate events as predicted by the MC vs the numbers of data events are provided by the lower rows.

CCQE enhanced sample composition		
MC reaction type	All E_ν	$E_\nu \leq 6$ GeV
ν_μ-CC QE	123, 310	120, 820
ν_μ-CC RES	41, 060	40, 110
ν_μ-CC DIS	21, 260	20, 580
ν_μ-CC COH	370	360
ν_μ-NC	420	420
$\bar{\nu}_\mu$	110	110
Total MC	186, 530	182, 400
Data	221, 300	216, 560
Data/MC ratio	1.186	1.187

In Table I and throughout this work, MC processes are labeled according to the interaction type that is "as born" inside the target nucleus. Thus signal events are events that originate as QE according to the MC, and the number of such events in the data is inferred from the MC. The topologies that emerge from the struck nucleus, however, are subject to alterations by final-state interactions. Among the as-born baryon resonance events (as-born DIS events), 28% (21%) are devoid of pions upon exiting the struck nucleus. These backgrounds are among the 73% of events in the simulated CCQE enhanced sample for which the final state released from the target nucleus consists solely of a muon plus nucleon(s).

C. Sample $E_\nu^{\rm QE}$ and $Q^2_{\rm QE}$ distributions

Comparisons of MC predictions to data are shown in Fig. 11 for $E_\nu^{\rm QE}$ and $Q^2_{\rm QE}$ distributions of the CCQE-enhanced sample; as with the sideband samples, the MC is plotted area-normalized to the data. The hatched component histograms show the extent to which the CCQE signal is expected to dominate the sample. In this figure and in subsequent comparisons, the suppression of baryon resonance production at low Q^2 is incorporated into the MC prediction as described in Sec. VIII C.

The analysis now focuses upon the $Q^2_{\rm QE}$ distribution of Fig. 11 (bottom); the remaining data-vs-MC discrepancies

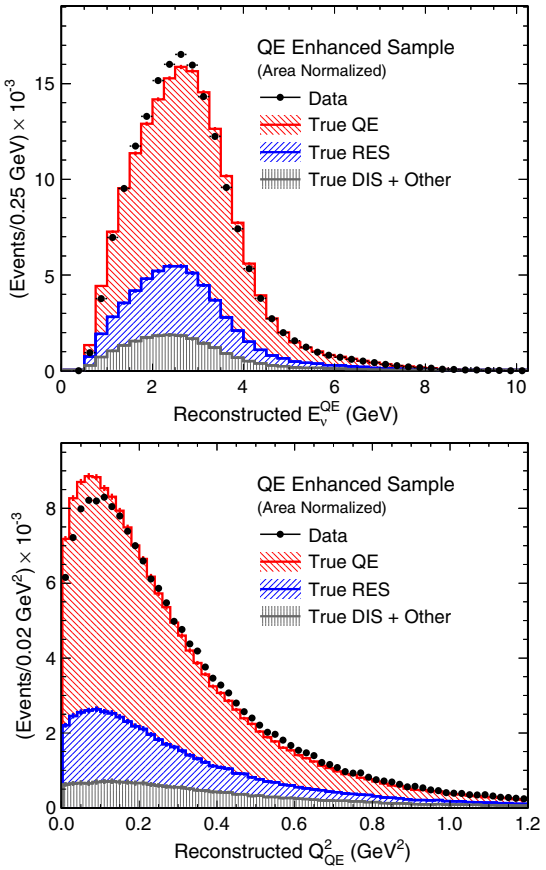

FIG. 11 (color online). Distributions of reconstructed neutrino energy, E_ν^{QE} (top), and of Q^2_{QE} (bottom) for CCQE selected data (solid circles) and for the flux-tuned MC (stacked histograms). The MC prediction includes the data-driven suppression weighting for CC baryon resonance production shown in Fig. 9. The MC distributions are scaled to match the data rate for Q^2_{QE} below 1.2 GeV^2. In the lower plot, the MC is observed to exceed (fall below) the data for Q^2_{QE} less than (greater than) 0.2 GeV^2.

are to be accounted for by fitting model parameters that alter the MC Q^2 distribution so as to better describe the data. The MC prediction (histogram, area-normalized) is observed to exceed the data (solid circles) in the region $0.0 < Q^2_{\mathrm{QE}} < 0.2$ GeV^2, and to fall below the data in all bins of the higher range $Q^2_{\mathrm{QE}} > 0.2$ GeV^2. The fit is capable of addressing these differences by determining the value of the axial mass M_A^{QE} that yields the best match of the MC to the data over the Q^2_{QE} range shown in Fig. 11. The discrepancy in the very low-Q^2 region indicates that the amount of Pauli blocking for CCQE events (governed by the k_{Fermi} parameter) is to be increased, while the differences at higher Q^2_{QE} suggest that M_A^{QE} values above 1.0 GeV are to be favored.

X. DETERMINATION OF EFFECTIVE M_A

As previously noted, the analysis foregoes the use of absolute event rate information. Rather, measurement of the effective M_A for quasielastic scattering in iron is based on the shape of the distribution of candidate CCQE events in the variable Q^2_{QE}.

A. Fit procedure

With the suppression weight now included in the MC modeling of CC baryon resonance production, the analysis focuses on the CCQE-enhanced sample and its distribution in reconstructed Q^2_{QE}, shown in the lower plot of Fig. 11. The modified MC prediction, with the axial-vector mass M_A treated as a free parameter, is to be fitted to the data. The fit is carried out by minimizing the following χ^2:

$$\chi^2 = \sum_{i=1}^{N_{\mathrm{bins}}} \frac{(N_i^{\mathrm{obs}} - N_i^{\mathrm{MC}}(M_A, \alpha_{j=1,3}))^2}{(N_i^{\mathrm{obs}} + r_0 \cdot N_i^{\mathrm{MC}}(M_A, \alpha_{j=1,3}))} + \sum_{k=1}^{3} \frac{(\Delta\alpha_k)^2}{\sigma^2_{\alpha_k}}. \tag{9}$$

Here, N_i^{obs} is the observed number of events in data for bin i, and $N_i^{\mathrm{MC}}(M_A, \alpha_1, \alpha_2, \alpha_3)$ is the number of events predicted by the MC using the current values of the fit parameter M_A and the three nuisance parameters, α_j for $j = 1, 2, 3$. The constant r_0 in the denominator is the ratio of POT in the data to POT in the MC. The MC prediction N_i^{MC} also contains a scale factor which sets the number of MC interactions equal to the number of data interactions. The latter factor is computed at the beginning of every trial fit and reduces the fit degrees of freedom by 1. Thus as the parameters change the number of MC events, the χ^2 evaluates the match to the shape of the data Q^2 distribution. The rightmost summation is over the penalty terms, each of which is the square of $\Delta\alpha_k$, the shift from nominal for the kth systematic parameter, divided by the square of σ_{α_k}, the 1σ error assigned to the kth systematic parameter.

The principal fit uses four parameters. The axial-vector mass, M_A, is the single free parameter. It is fitted in conjunction with three nuisance parameters: (i) A scale parameter for the momentum assignment to stopping muons for which $\pm1\sigma$ corresponds to $\pm2\%$ [36]; (ii) the axial-vector mass for CC baryon resonance production, M_A^{RES}, having nominal value 1.12 GeV with uncertainty (at 1σ) of $\pm15\%$ [36,51]; and (iii) the Fermi momentum cutoff, k_{Fermi}, whose value (263 MeV/c for neutrons in iron) is used by NEUGEN3 to set the strength of Pauli blocking for CCQE interactions within target nuclei.

The k_{Fermi} cutoff acts as an effective low-Q^2_{QE} suppression parameter. It serves the same purpose as the κ parameter used by MiniBooNE [3,5]. The parameter provides the fit with a proxy equivalent for a treatment of Pauli blocking plus other nuclear effects that are operative at low Q^2_{QE}. In NEUGEN3, the CCQE kinematics are computed for all possible four-momentum transfers. However generated events having recoil nucleon momenta below the k_{Fermi} limit are rejected. Based on comparisons with models using nuclear spectral functions [69] or using

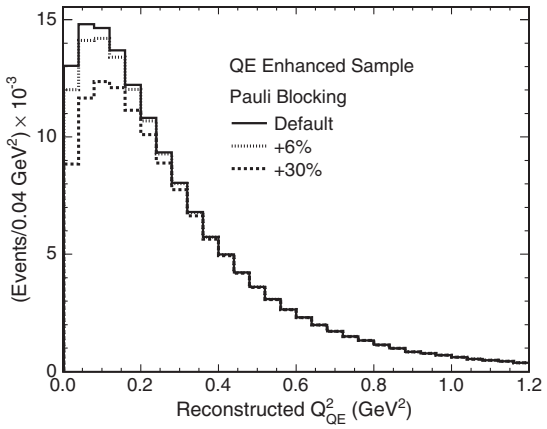

FIG. 12. Enhanced suppression of the MC $Q^2_{\rm QE}$ distribution for the CCQE enhanced sample resulting from an increase in the upper momentum cutoff for nucleons in iron, $k_{\rm Fermi}$, above its nominal value of 263 MeV/c. The bold-dashed histogram shows the effect of setting $k_{\rm Fermi}$ at the upper bound of plausible values. The principal fit of this analysis favors the milder suppression shown by the fine-dashed histogram.

RDWIA [70], additional amounts of suppression produced by increasing $k_{\rm Fermi}$ by as much as 30% are possible in theory. The viability of this elevated parameter range is also supported by comparisons to current models with RPA effects [24,26,29,30], and by the resonance suppression results described in Sec. VIII C. For these reasons $k_{\rm Fermi}$ is allowed to vary above its nominal in accordance with a 1σ uncertainty of 30% during iterations of the principal fit. The range of low-$Q^2_{\rm QE}$ suppression in CCQE accessible via $k_{\rm Fermi}$ is illustrated by the lowest (bold-dashed) histogram in Fig. 12. As it turns out (see paragraphs below), the principal fit requires a relatively small amount of additional suppression, from a $k_{\rm Fermi}$ increase of +6%, to describe the data. The low-Q^2 suppression thereby implied to the $Q^2_{\rm QE}$ distribution of the CCQE enhanced sample is shown in Fig. 12 by the fine-dashed histogram.

B. Fitting the shape of the $Q^2_{\rm QE}$ distribution

Since the MC vs data comparisons of Sec. IX C have shown the low-$Q^2_{\rm QE}$ regime to be poorly modeled, the fitting of the reconstructed $Q^2_{\rm QE}$ distribution of the CCQE-enriched sample was carried out using two different configurations. For each configuration, the fitting of the augmented MC prediction to the data is only for the shape of the $Q^2_{\rm QE}$ distribution; an upper bound of 1.2 GeV^2 is imposed on $Q^2_{\rm QE}$ for events of either fit.

In the principal fit, all events having reconstructed $Q^2_{\rm QE}$ less than 1.2 GeV^2 were included and the $k_{\rm Fermi}$ parameter was allowed to vary. The best-fit values thereby obtained are given in the upper row of Table II. The principal fit yields a reduced χ^2 per degree of freedom of 0.79; the uncertainty on the best-fit M_A value due solely to statistical effects is ± 0.07 GeV.

TABLE II. Results from shape-only fits to the $Q^2_{\rm QE}$ distribution of the selected CCQE sample, for M_A, for the three nuisance parameters, and the MC to data normalization obtained with the best-fit parameters. The fit over the full reconstructed $Q^2_{\rm QE}$ range (upper row) is compared to a fit in which the $Q^2_{\rm QE}$ region most susceptible to nuclear distortions is left out (lower row).

$Q^2_{\rm QE}$ range (GeV^2)	M_A (GeV)	E_μ scale	$M_A^{\rm RES}$ (GeV)	$k_{\rm Fermi}$ scale
0.0–1.2	$1.23^{+0.13}_{-0.09}$	1.00 ± 0.01	$1.09^{+0.14}_{-0.15}$	1.06 ± 0.02
0.3–1.2	$1.22^{+0.18}_{-0.11}$	$1.00^{+0.01}_{-0.02}$	$1.09^{+0.15}_{-0.16}$	N.A.

For the alternate configuration, only CCQE candidates having reconstructed $Q^2_{\rm QE}$ values between 0.3 GeV^2 and 1.2 GeV^2 were used, and the normalization of MC events to data was restricted to this reduced Q^2 range. Furthermore, the $k_{\rm Fermi}$ parameter was fixed at its nominal value. As in all previous fit trials, low-Q^2 suppression of CC baryon resonance production is operative in the MC model. A good fit to the data is obtained, indicating that the modeling augmentations at low Q^2 contribute to the agreement between MC and data obtained by this more restricted fit. The values for the axial-vector mass, M_A, and for the three nuisance parameters describing the systematics are shown in the lower row of Table II; these are in excellent agreement with the results of the principal fit.

Concerning the absolute rate of events in the CCQE enhanced sample (not used in the fits), the fit results imply $[N_{\rm data}/N_{\rm MC}]_{\rm CCQE} = 1.09$. This value is an improvement compared to the ratio 1.19 predicted by the original MC model (see Table I).

Comparisons of the default (dotted-line histogram) and best-fit (solid-line histogram) MC $Q^2_{\rm QE}$ spectra to the data distribution are presented in Fig. 13. The matchup of distributions is shown in the upper plot, and the ratio of the data to the predicted MC distribution is displayed in the lower plot. In the upper plot, the principal fit (upper row of Table II) is seen to provide an excellent description of the data distribution over the full range of $Q^2_{\rm QE}$ considered by this analysis. This is not the case for the original reference MC. As is apparent in Fig. 13 (top) and is made explicit by the ratio displayed in Fig. 13 (bottom), the shape predicted by the reference MC describes a spectrum that lies above the data for $Q^2 < 0.15$ GeV^2 and falls below the data for $Q^2 > 0.25$ GeV^2.

C. Systematic errors for determination of M_A

The principal fit treats three sources of uncertainty using nuisance parameters whose values *ab initio* are known to within certain ranges. There are, however, systematic uncertainties whose contribution cannot be captured in that way. These include errors inherent to the event reconstruction, to the analysis procedure, and to model uncertainties. The approach taken here is to set the relevant

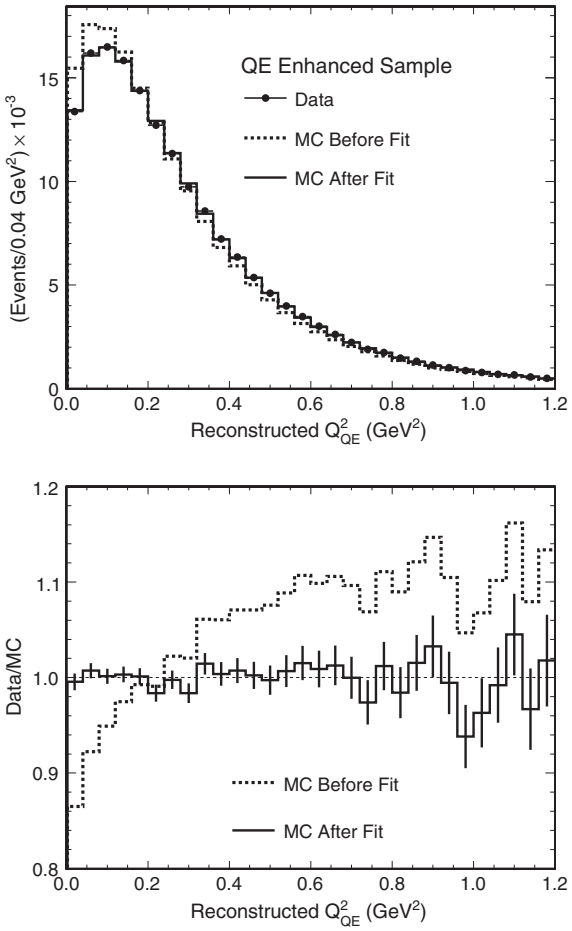

FIG. 13. MC predictions (dotted, solid-line histograms) compared to the distribution of reconstructed $Q^2_{\rm QE}$ for events of the CCQE enhanced sample (solid circles). The plots show that the best-fit MC, which is fitted to the shape of the data distribution over the range of allowed $Q^2_{\rm QE}$, agrees very well with the data (top, solid-line vs data points). For the best-fit MC, the data-over-MC ratio (bottom, solid-line histogram) equals 1.0 to within $\pm 4\%$ in all bins over the full Q^2 range.

event selection or model parameter to its $\pm 1\sigma$ values and then to refit the MC to the CCQE enhanced data sample. The deviations ($\pm$) in best-fit M_A which result from the variations comprise the error estimate to the M_A determination arising from a particular systematic. There are eight sources of systematic error whose individual contribution to the error budget is comparable to statistical fluctuations. Their identity and evaluation are described below, in descending order of estimated error contribution:

(1) *Intranuclear scattering of produced hadrons*: Pions and nucleons produced in the initial νN interactions in iron can reinteract within the nucleus before emerging to produce the observed final state. Their alteration of final states is accounted for by NEUGEN3 using an intranuclear cascade model. The model contains parameters which govern the effective cross sections for pion and nucleon rescattering. The parameters are set according to published data on νN, γN, and πN scattering; however each parameter has an error range. Changes in these parameters cause event migrations in the MC across the $E_{\rm had}$ selection that defines the CCQE sample [72]. In a detector where a large fraction of the target material is passive, events are moved into and out of the $E_{\rm had} \simeq 0$ region (see Fig. 3).

Trial fits were carried out in which the MC was reweighted to simulate a $\pm 1\sigma$ change to an intranuclear scattering parameter [73]; separate trials were carried out for each of the ten parameters. For all trials the best-fit values for M_A and for the nuisance parameters were observed to remain within the 1σ error range of the nominal value. The main uncertainties are associated with nucleon absorption, pion absorption, and with the hadron formation time. (The formation time determines the point at which a produced hadron acquires its full scattering cross section.) Uncertainties with other parameters are either negligible or strongly correlated with the errors of these three processes. The quadrature sum from the individual (maximum magnitude) variations to M_A induced by parameter variations for these three intranuclear rescattering processes is taken as the overall error estimate listed in the first row of Table III.

(2) *CCQE selection using visible hadronic energy*: The primary CCQE selection requires the reconstructed energy of the hadronic system recoiling from the muon to be less than 225 MeV. This cut removes most CC DIS events since these processes tend to have relatively large $E_{\rm had}$ values. It also reduces the amount of CC baryon resonance production which remains as a background. The cut value chosen lies at the midpoint of an $E_{\rm had}$ range characterized by small and regular changes in sample purity and in MC-vs-data discrepancy with incremental variation in $E_{\rm had}$. This region of relative stability extends for

TABLE III. Shift from nominal in the value of M_A resulting from variation of each systematic error source. The systematics listed here are evaluated separately from the nuisance parameters of the principal fit.

	Fit Q^2 range $0.0 < Q^2_{\rm QE} < 1.2$ GeV^2	
Systematic error source	(+) shift (GeV)	(−) shift (GeV)
Intranuclear scattering	0.066	0.066
CCQE $E_{\rm had}$ selection	0.062	0.062
Detector model in x, z	0.059	0.059
$\Delta/{\rm N}^*$ low-Q^2 suppression	0.005	0.088
Hadronic energy offset	0.047	0.045
DIS cross section	0.024	0.022
μ^- angular resolution	0.016	0.015
Flux-tuning parameters	0.008	0.008
Total syst. error (GeV)	+0.122	−0.149

± 75 MeV on either side of the designated cut value at 225 MeV. The uncertainty inherent to placement of the cut is evaluated using a set of trial fits of the MC to data in which the assigned $E_{\rm had}$ cut value is stepped from 150 to 300 MeV. The maximum variation in the fit outcomes provides the error estimate (second row of Table III).

(3) *Uncertainties in detector modeling*: The detector is divided longitudinally (z-coordinate) into calorimeter and spectrometer sections. The analysis fiducial volume is located asymmetrically with respect to the detector's transverse, horizontal dimension (x-coordinate) and with respect to the toroidal magnetic field. In trial fits using subsamples selected from different regions of the fiducial volume, small shifts of fit parameter values are observed which correlate with event vertex location. These shifts have a nonstatistical component and appear to be associated with uncertainties in detector modeling. Their presence implies a systematic uncertainty for the M_A measurement. An error estimate is obtained by relating excursions observed in E_μ and θ_μ to corresponding trends in Q^2, and then evaluating the variation that propagates to the M_A determination. Excursions of potential significance are observed with sample splitting based upon vertex z or upon vertex x. On the other hand negligible variations are found when splitting the sample according to vertex y; the distribution of event vertices exhibits vertical symmetry in the fiducial region, as expected. The excursions associated with sample subdivisions using vertex z or vertex x imply shifts propagated to M_A of 4.0% and 3.3% respectively. The uncertainty assigned to the best-fit value of the M_A measurement is taken as the quadrature sum.

(4) *Low-Q^2 suppression of baryon resonance production*: A suppression weight has been added to the MC modeling of CC baryon resonance production at low Q^2, as described in Sec. VIII C. A systematic error is assigned to the utilization of this weight. It represents uncertainties associated with the shape of the weight function, in particular with its representation of the approach to null suppression as a function of increasing Q^2. The error is estimated by shifting the suppression function in accordance with its $\pm 1\sigma$ error band and then refitting to find the resulting variation in M_A (fourth row, Table III).

(5) *Hadronic energy MC-vs-data offset*: Discrepancies may exist between energies assigned to visible hadronic activity in data vs the MC at the level of tens of MeV. Sources include offsets in the calorimeter response to stopping pions and/or protons and the data-vs-MC difference in the effect of nucleon binding energy on reconstructed $E_{\rm had}$. Such offsets cause a small migration of MC events across the $E_{\rm had}$ selection boundary. For the above-mentioned sources, an upper bound of 20 MeV is estimated for the magnitude of the net offset. On the basis of trial fits in which the $E_{\rm had}$ cut for the MC was varied by ± 20 MeV, the uncertainty propagated to M_A was ascertained.

(6) *CC DIS cross section*: Approximately 11% of the CCQE enhanced sample consists of CC DIS events. In the MC, the DIS cross section for scattering into low-multiplicity pion production channels is implemented by a combination of KNO and Bodek-Yang [52] models. The relative cross section rates, among CC channel combinations of the target nucleon with multiple charged and neutral pions, are governed by a parameter set which, upon introduction of isospin constraints, reduces to four parameters. Uncertainty ranges are assigned to these parameters by NEUGEN3 on the basis of limited knowledge of the cross sections. The sensitivity of DIS contributions to the sideband samples is not sufficient to further constrain these errors. Fit trials were conducted in which the parameters were varied individually over their $\pm 1\sigma$ ranges and the fit to M_A was redone. The maximum M_A displacement for each parameter was added in quadrature to obtain the estimated systematic error. The dominant contribution to this error arises from cross section uncertainties with CC two-pion channels.

(7) *Correction to muon angular resolution in the MC*: As described in Sec. VII B, a $Q^2_{\rm QE}$-dependent weight is applied to MC events of the CCQE enhanced sample to ensure that muon angular resolution of the MC represents the resolution observed in the data. The required correction is found to be nearly identical across all subsamples of the analysis; the method of correction is insensitive to the underlying M_A in a sample. The determination of the MC-vs-data resolution difference per bin of muon track length has uncertainties, and these define the error envelope associated with the correction weight applied to MC events. The one-sigma variations allowed by the envelope impart an uncertainty to the M_A determination of the amount shown in row 7 of Table III.

(8) *NuMI flux-tuning parameters*: The NuMI flux calculation used by the MC includes tuned parameter settings that characterize the beam optics and the production of hadrons from the primary target [36]. Changes of $\pm 1\sigma$ are considered for each beam-optics parameter; also considered are the differences between calculated vs data-tuned settings for the hadro-production parameters. By design, the analysis is insensitive to the absolute scale of the neutrino flux, and the distribution shape for $Q^2_{\rm QE}$ is also fairly

insensitive to uncertainties in the spectral shape of the neutrino flux. Consequently these flux uncertainties give a subpercent contribution to the systematic error budget.

For each error source in Table III (left-hand column), the shifts in the axial-vector mass from the best-fit nominal value (lower row of Table II) are presented in the second and third columns of Table III for systematic parameter variations of $+1\sigma$ and -1σ respectively. The bottom row displays the quadrature sums of the systematic errors. The sums represent the systematic error contribution arising from all sources other than those treated by the nuisance parameters of the principal fit.

The QE-enhanced data sample is essentially a CC single-track sample, and the requirement that the detected hadronic system be of zero or low energy is central to the event selection. Table III shows that uncertainties associated with the selection of $E_{\rm had}$ (rows 2 and 5) contribute significantly to the systematic error. These errors, together with the contribution from intranuclear rescattering (row 1), are intrinsic to the use of thick iron plates in the detector. Similarly, the uncertainties associated with detector modeling arise from asymmetries in the detector configuration and are not amenable to significant further reduction.

XI. RESULTS AND DISCUSSION

Charged current ν_μFe interactions initiated by a broad-band neutrino flux peaked at ~3.0 GeV are examined with high statistics using a three-stage analysis. In the first stage, final states are examined inclusively using distributions in visible hadronic energy, neutrino energy, Q^2, and in hadronic mass W. A conventional MC model using a RFG nucleus and with CCQE scattering, baryon-resonance production, and inelastic scattering/DIS as the predominant interaction categories, is found to give rough but respectable characterizations of the data (Figs. 3, 4, and 5).

This characterization guides the second stage in which the CC inclusive sample is broken out into independent subsamples, each containing a distinctive mixture of the three main reaction categories. One subsample, selected to be enriched in CCQE events, is put aside for the third stage. The remaining four subsamples are dominated by baryon-resonance and inelastic/DIS events. The shapes of data Q^2 distributions for the latter samples are then compared to the MC model (Figs. 6, 7, and 8).

Here also the MC manages respectable description by and large; however at low Q^2 its predictions exceed the data in subsamples containing sizable amounts of baryon-resonance production [of mostly $\Delta(1232)$ states]. Motivated by this correlation, and with knowledge of the evidence given by MiniBooNE for baryon-resonance suppression in neutrino-carbon interactions at low Q^2 [5,64,65], a suppression function is developed whose Q^2 dependence is displayed in Fig. 9. The analysis incorporates this low-Q^2 suppression of baryon resonances into its otherwise conventional MC treatment of neutrino-nucleus scattering for the purpose of fitting the CCQE-enriched subsample.

The CCQE enhanced subsample is the focus of the analysis third stage. Its distribution in $Q^2_{\rm QE}$, for neutrinos of $1.0 < E_\nu < 8.0$ GeV, is presented in Fig. 13. This sample contains 221, 297 events of which 66% are estimated to be quasielastic interactions (see Table I). The shape of the $Q^2_{\rm QE}$ distribution of the CCQE-enriched data sample is fitted using a χ^2 in which the axial-vector mass M_A is a free parameter, and the muon energy scale, the axial-vector mass for baryon resonance production, and an effective low-$Q^2_{\rm QE}$ suppression are treated using nuisance parameters. For the effective M_A value which sets the Q^2 scale in the empirical dipole axial-vector form factor of neutrons bound within iron nuclei, the best-fit value is

$$M_A = 1.23^{+0.13}_{-0.09}(\text{fit})^{+0.12}_{-0.15}(\text{syst})\ \text{GeV}. \tag{10}$$

The mean neutrino energy for the fitted signal sample is $\langle E_\nu \rangle = 2.79$ GeV. The error range obtained by the fit includes the effects of finite sample statistics plus the variations and correlations allowed by the nuisance parameters. The uncertainty introduced by the systematic error sources is additional to that which is estimated by the fit. It is listed separately in Eq. (10).

The best-fit MC result, as shown in Fig. 13, gives an excellent description of the shape of the data $Q^2_{\rm QE}$ distribution over the range $0.0 < Q^2_{\rm QE} < 1.2$ GeV^2. Compared to the original MC reference model, the data prefer a Q^2 spectrum which is harder (flatter) through this range. As shown in Fig. 12, the data also prefer that a small amount of additional rate suppression be added at low Q^2.

As related in Sec. III, the axial-vector mass of CCQE scattering on free nucleons is generally regarded to be ~30–40 MeV lower than the 2002 compilation value (1.026 ± 0.021) GeV of Ref. [17]. The effective M_A value for CCQE interactions in iron nuclei determined by this analysis lies above the free-nucleon value, although with allowance for systematic uncertainty the disagreement is only at the level of 1.4σ. Table III shows that no single source dominates the systematic error assigned to M_A; hence further reduction of the total error would be difficult to accomplish with MINOS data. Among the five leading systematics there are four arising from the near detector which was originally designed for measurement of ν_μ disappearance due to oscillations.

The MINOS effective M_A value is in agreement with the K2K result for interactions in oxygen: $M_A = (1.20 \pm 0.12)$ GeV [1]. It is also compatible with the relatively high nominal value obtained by MiniBooNE for CCQE interactions on carbon: $M_A = (1.35 \pm 0.17)$ GeV [5]. Notable perhaps with the MINOS result is the absence of an upward trend in effective M_A when a distinctly larger target nucleus is used. The MINOS value, together with the K2K and MiniBooNE results, are consistent with

interpretations [10,21,24,30] that large values for the effective M_A reflect nuclear medium effects not accounted for using the Fermi gas treatment of the nucleus. On the other hand, the value presented in Eq. (10) lies above the NOMAD measurement for high energy ν_μ-carbon scattering: $M_A = (1.05 \pm 0.06)$ GeV [4]. Their result is based upon a combined sample of 1-track and 2-track events with $3 < E_\nu < 100$ GeV and with Q^2 extending to 2.0 GeV^2.

In summary, an investigation of CC ν_μ interactions on iron is reported which bridges the neutrino energy ranges previously examined by experiments using light-nucleus targets. Event distributions in kinematic variables are presented for CC inclusive scattering, and for subsamples selected to have distinctly different populations of CCQE, baryon resonance production, and inelastic/DIS events. For all distributions, comparisons are given to predictions of a MC simulation based upon conventional phenomenology with neutrinos interacting with quasifree nucleons in a nucleus modeled as a relativistic Fermi gas. From these comparisons it is inferred that CC baryon resonance production, the principal background to CCQE, is subject to a Q^2-dependent suppression of rate with the functional form shown in Fig. 9. With inclusion of this suppression effect into the MC simulation, the Q^2 distribution for CCQE scattering in iron is found to be well described using an effective axial-vector mass with the value given in Eq. (10).

These results provide new information for development of more realistic models of charged-current neutrino-nucleus scattering and of nuclear medium effects at work in CCQE and CC baryon resonance production. Improved models are needed as benchmarks for interpreting neutrino scattering data and as guides to precise determinations of the atmospheric mixing angle and of other neutrino oscillation parameters [11].

ACKNOWLEDGMENTS

This work was supported by the U.S. DOE; the U.K. STFC; the U.S. NSF; the State and University of Minnesota; the University of Athens, Greece; and Brazil's FAPESP, CAPES, and CNPq. We thank the staff of Fermilab for their invaluable contributions to the research of this work.

[1] R. Gran *et al.* (K2K Collaboration), Phys. Rev. D **74**, 052002 (2006).
[2] X. Espinal and F. Sanchez, AIP Conf. Proc. **967**, 117 (2007).
[3] A. A. Aguilar-Arevalo *et al.* (MiniBooNE Collaboration), Phys. Rev. Lett. **100**, 032301 (2008).
[4] V. Lyubushkin *et al.* (NOMAD Collaboration), Eur. Phys. J. C **63**, 355 (2009).
[5] A. A. Aguilar-Arevalo *et al.* (MiniBooNE Collaboration), Phys. Rev. D **81**, 092005 (2010).
[6] Y. Nakajima *et al.* (SciBooNE Collaboration), Phys. Rev. D **83**, 012005 (2011).
[7] K. Abe *et al.* (T2K Collaboration), Phys. Rev. D **87**, 092003 (2013).
[8] L. Fields *et al.* (MINERνA Collaboration), Phys. Rev. Lett. **111**, 022501 (2013).
[9] G. A. Fiorentini *et al.* (MINERνA Collaboration), Phys. Rev. Lett. **111**, 022502 (2013).
[10] H. Gallagher, G. Garvey, and G. P. Zeller, Annu. Rev. Nucl. Part. Sci. **61**, 355 (2011).
[11] P. Coloma and P. Huber, Phys. Rev. Lett. **111**, 221802 (2013).
[12] A study of quasielastic scattering in iron plates conducted at ANL was published in 1969: R. L. Kustom, D. Lundquist, T. Novey, A. Yokosawa, and F. Chilton, Phys. Rev. Lett. **22**, 1014 (1969).
[13] H. Gallagher, Nucl. Phys. B, Proc. Suppl. **112**, 188 (2002).
[14] C. H. Llewellyn-Smith, Phys. Rep. **3**, 261 (1972).
[15] R. P. Feynman and M. Gell-Mann, Phys. Rev. **109**, 193 (1958).
[16] R. G. Sachs, Phys. Rev. Lett. **12**, 231 (1964).
[17] V. Bernard, L. Elouadrhiri, and U.-G. Meissner, J. Phys. G **28**, R1 (2002).
[18] K. L. Miller *et al.*, Phys. Rev. D **26**, 537 (1982).
[19] T. Kitagaki *et al.*, Phys. Rev. D **42**, 1331 (1990).
[20] K. S. Kuzmin, V. V. Lyubushkin, and V. A. Naumov, Eur. Phys. J. C **54**, 517 (2008).
[21] J. G. Morfin, J. Nieves, and J. T. Sobczyk, Adv. High Energy Phys. **2012**, 934597 (2012).
[22] A. Bodek, H. Budd, and M. Christy, Eur. Phys. J. C **71**, 1726 (2011); see also Refs. [27] and [29] of this Paper.
[23] J. Nieves, J. E. Amaro, and M. Valverde, Phys. Rev. C **70**, 055503 (2004); **72**, 019902(E) (2005).
[24] M. Martini, M. Ericson, G. Chanfray, and J. Marteau, Phys. Rev. C **80**, 065501 (2009).
[25] M. Martini, M. Ericson, G. Chanfray, and J. Marteau, Phys. Rev. C **81**, 045502 (2010).
[26] M. Martini, M. Ericson, and G. Chanfray, Phys. Rev. C **84**, 055502 (2011).
[27] J. E. Amaro, M. B. Barbaro, J. A. Caballero, T. W. Donnelly, and C. F. Williamson, Phys. Lett. B **696**, 151 (2011).
[28] G. D. Megias, J. E. Amaro, M. B. Barbaro, J. A. Caballero, and T. W. Donnelly, Phys. Lett. B **725**, 170 (2013).
[29] J. Nieves, I. Ruiz Simo, and M. J. Vicente Vacas, Phys. Lett. B **707**, 72 (2012).
[30] R. Gran, J. Nieves, F. Sanchez, and M. J. Vicente Vacas, Phys. Rev. D **88**, 113007 (2013).
[31] J. Nieves, I. Ruiz Simo, and M. J. Vicente Vacas, Phys. Rev. C **83**, 045501 (2011).
[32] B. G. Tice *et al.* (MINERνA Collaboration), Phys. Rev. Lett. **112**, 231801 (2014).

[33] K. Anderson *et al.*, Report No. FERMILAB-DESIGN-1998-01, 1998.
[34] A. Ferrari, P. R. Sala, A. Fasso, and J. Ranft, Report No. CERN-2005-010, Report No. INFN/TC_05/11, Report No. SLAC-R-773, 2005.
[35] R. Brun *et al.*, CERN Program Library, Long Writeup W5013, 1994.
[36] P. Adamson *et al.* (MINOS Collaboration), Phys. Rev. D **77**, 072002 (2008).
[37] P. Adamson *et al.* (MINOS Collaboration), Phys. Rev. D **81**, 072002 (2010).
[38] D. G. Michael *et al.* (MINOS Collaboration), Nucl. Instrum. Methods Phys. Res., Sect. A **596**, 190 (2008).
[39] M. Dorman, Report No. MINOS doc-4869, 2008 (unpublished).
[40] P. Adamson *et al.*, Nucl. Instrum. Methods Phys. Res., Sect. A **556**, 119 (2006).
[41] A. Cabrera *et al.*, Nucl. Instrum. Methods Phys. Res., Sect. A **609**, 106 (2009).
[42] C. Andreopoulos *et al.*, Nucl. Instrum. Methods Phys. Res., Sect. A **614**, 87 (2010).
[43] D. Casper, Nucl. Phys. B, Proc. Suppl. **112**, 161 (2002).
[44] Y. Hayato, Nucl. Phys. B, Proc. Suppl. **112**, 171 (2002); Acta Phys. Pol. B **40**, 2477 (2009).
[45] C. Juszczak, J. A. Nowak, and J. T. Sobczyk, Nucl. Phys. B, Proc. Suppl. **159**, 211 (2006).
[46] R. Bradford, A. Bodek, H. Budd, and J. Arrington, Nucl. Phys. B, Proc. Suppl. **159**, 127 (2006).
[47] A. Bodek and J. L. Ritchie, Phys. Rev. D **23**, 1070 (1981).
[48] O. Benhar, A. Fabrocini, S. Fantoni, and I. Sick, Nucl. Phys. **A579**, 493 (1994).
[49] R. Merenyi, W. A. Mann, T. Kafka, W. Leeson, B. Saitta, J. Schneps, M. Derrick, and B. Musgrave, Phys. Rev. D **45**, 743 (1992).
[50] D. Rein and L. Seghal, Ann. Phys. (N.Y.) **133**, 79 (1981).
[51] K. S. Kuzmin, V. V. Lyubushkin, and V. A. Naumov, Acta Phys. Pol. B **37**, 2337 (2006).
[52] A. Bodek and U. K. Yang, AIP Conf. Proc. **721**, 358 (2004).
[53] T. Yang, C. Andreopoulos, H. Gallagher, and P. Kehayias, AIP Conf. Proc. **967**, 269 (2007).
[54] Z. Koba, H. B. Nielsen, and P. Olesen, Nucl. Phys. **B40**, 317 (1972).
[55] T. Sjostrand, S. Mrenna, and P. Skands, J. High Energy Phys. 05 (2006) 026.
[56] D. Rein and L. Seghal, Nucl. Phys. **B223**, 29 (1983).
[57] P. Adamson *et al.* (MINOS Collaboration), Phys. Rev. Lett. **101**, 131802 (2008).
[58] R. Ospanov, Ph. D. Thesis, University of Texas, Austin, 2008 [Report No. FERMILAB-THESIS-2008-04].
[59] L. Aliaga *et al.* (MINERνA Collaboration), Nucl. Instrum. Methods Phys. Res., Sect. A **743**, 130 (2014).
[60] N. Graf, R. Gran, T. Kafka, W. A. Mann, N. Mayer, and S. G. Wojcicki, Report No. MINOS doc-9470, 2014 (unpublished).
[61] M. Dorman, Ph. D. Thesis, University College, London, 2008 [Report No. FERMILAB-THESIS-2008-72].
[62] D. Harris, "Constraining the NuMI flux," in NuInt14, 2014 (to be published).
[63] A. Korzenev, "Hadron production experiments to constrain the neutrino flux," in NEUTRINO 2014, 2014.
[64] A. A. Aguilar-Arevalo *et al.* (MiniBooNE Collaboration), Phys. Rev. D **83**, 052007 (2011).
[65] A. A. Aguilar-Arevalo *et al.* (MiniBooNE Collaboration), Phys. Rev. D **83**, 052009 (2011).
[66] E. A. Paschos, M. Sakuda, I. Schienbein, and J. Y. Yu, Nucl. Phys. B, Proc. Suppl. **139**, 125 (2005).
[67] J. Marteau, Eur. Phys. J. A **5**, 183 (1999).
[68] K. M. Graczyk and J. T. Sobczyk, Eur. Phys. J. C **31**, 177 (2003).
[69] O. Benhar and D. Meloni, Phys. Rev. D **80**, 073003 (2009).
[70] A. V. Butkevich, Phys. Rev. C **78**, 015501 (2008).
[71] N. Graf and R. Gran, Report No. MINOS doc-7684, 2010 (unpublished).
[72] S. Dytman, H. Gallagher, and M. Kordosky, *Proc. Sci.*, NuFACT08 (2008) 041.
[73] H. Gallagher, Acta Phys. Pol. B **40**, 2607 (2009).